

Sea Ice Rheology Experiment (SIREx), Part I: Scaling and statistical properties of sea-ice deformation fields

Amélie Bouchat¹, Nils Hutter², Jérôme Chanut³, Frédéric Dupont⁴, Dmitry Dukhovskoy⁵, Gilles Garric³, Younjoo Lee⁶, Jean-François Lemieux⁷, Camille Lique⁸, Martin Losch², Wieslaw Maslowski⁶, Paul G. Myers⁹, Einar Ólason¹⁰, Pierre Rampal¹¹, Till Rasmussen¹², Claude Talandier⁸, Bruno Tremblay¹, Qiang Wang²

¹Department of Atmospheric and Oceanic Sciences, McGill University, Montréal, QC, Canada.

²Alfred-Wegener-Institut, Helmholtz Zentrum für Polar- und Meeresforschung, Bremerhaven, Germany.

³Mercator Ocean International, Ramonville-Saint-Agne, France

⁴Service Météorologique Canadien, Environnement et Changement Climatique Canada, Dorval, Qc, Canada

⁵Center for Ocean-Atmospheric Prediction Studies, Florida State University, Tallahassee, FL, USA

⁶Department of Oceanography, Naval Postgraduate School, Monterey, California, USA

⁷Recherche en Prévision Numérique Environnementale, Environnement et Changement Climatique Canada, Dorval, Qc, Canada

⁸University of Brest, CNRS, IRD, Ifremer, Laboratoire d'Océanographie Physique et Spatiale (LOPS), IUEM, Brest, France

⁹Department of Earth and Atmospheric Sciences, University of Alberta, Edmonton, Alberta, Canada

¹⁰Nansen Environmental and Remote Sensing Centre, and Bjerknes Centre for Climate Research, Bergen, Norway

¹¹Institut de Géophysique de l'Environnement, CNRS, Grenoble, France

¹²Danish Meteorological Institute, Copenhagen, Denmark

Key Points:

- Power-law scaling and multi-fractality of deformations in space and time can be achieved by both plastic and brittle sea-ice rheologies.
- Scaling statistics of simulated sea-ice deformation fields depend on the model configuration and physical parameterizations.
- Finite-difference plastic models need to be run at higher resolution than that of observations for deformation statistics to agree with observations.

Corresponding author: Amélie Bouchat, amelie.bouchat@mail.mcgill.ca

Abstract

As the sea-ice modeling community is shifting to advanced numerical frameworks, developing new sea-ice rheologies, and increasing model spatial resolution, ubiquitous deformation features in the Arctic sea ice are now being resolved by sea-ice models. Initiated at the Forum for Arctic Modelling and Observational Synthesis (FAMOS), the Sea Ice Rheology Experiment (SIREx) aims at evaluating current state-of-the-art sea-ice models using existing and new metrics to understand how the simulated deformation fields are affected by different representations of sea-ice physics (rheology) and by model configuration. Part I of the SIREx analysis is concerned with evaluation of the statistical distribution and scaling properties of sea-ice deformation fields from 35 different simulations against those from the RADARSAT Geophysical Processor System (RGPS). For the first time, the Viscous-Plastic (and the Elastic-Viscous-Plastic variant), Elastic-Anisotropic-Plastic, and Maxwell-Elasto-Brittle rheologies are compared in a single study. We find that both plastic and brittle sea-ice rheologies have the potential to reproduce the observed RGPS deformation statistics, including multi-fractality. Model configuration (e.g. numerical convergence, atmospheric forcing, spatial resolution) and physical parameterizations (e.g. ice strength parameters and ice thickness distribution) both have effects as important as the choice of sea-ice rheology on the deformation statistics. It is therefore not straightforward to attribute model performance to a specific rheological framework using current deformation metrics. In light of these results, we further evaluate the statistical properties of simulated Linear Kinematic Features (LKFs) in a SIREx Part II companion paper.

Plain Language Summary

The ice in the Arctic Ocean is not continuous: it breaks under the influence of winds and ocean currents. The fractures in the ice pack form zones of intense deformations, where important energy exchanges between the atmosphere and ocean take place. To simulate these deformations and include realistic ice dynamics in climate projections, different sea-ice models have been proposed. The goal of the Sea Ice Rheology Experiment (SIREx) is to compare these different models and assess how realistic are the simulated deformations compared to those derived from satellite observations. SIREx is divided in two parts. In Part I (this study), we compare statistical properties of the deformation fields, as characterized by their intensity distribution. In our companion paper for Part II, we compare the sea-ice deformation fields through statistics of linear deformation features that are apparent in both observations and simulations. We show that current sea-ice models can reproduce realistic deformation statistics, without preference for a given fracturing or deformation model. We also suggest new methods for comparing models with observations, and we formulate recommendations for configuring more realistic sea-ice simulations.

1 Introduction

Statistical properties of small-scale sea-ice dynamics derived from buoy records and synthetic aperture radar (SAR) imagery in the Arctic Ocean have been extensively documented in the last two decades. Observations from the RADARSAT Geophysical Processor System (RGPS) show that deformations in shear and divergence (positive and negative) define highly-localized Linear Kinematic Features (LKF — e.g. Kwok, 2001) and complex spatio-temporal scaling laws describe their localization over a wide range of spatial and temporal scales (Marsan et al., 2004; Rampal et al., 2008; Stern & Lindsay, 2009; Marsan & Weiss, 2010). Specifically, the mean total deformation rates follow a power-law with increasing spatial and temporal scales and the scaling exponent of this power-law increases non-linearly when considering higher moments of the deformation distribution, suggesting that very large deformation rates significantly affect the mean deformation statistics (Weiss & Dansereau, 2017; Rampal et al., 2019). These properties are reminiscent of fully-turbulent flows, which also exhibit strong heterogeneity and intermittency and are characterized as multi-fractal processes (e.g. Benzi et al., 1984; Schmitt et al., 1994). As such, the observed sea-ice deformation characteristics might provide meaningful information about the underlying mechanisms governing the sea-ice mechanics. For example, the highly-localized LKFs have been hypothesized to result from brittle compressive shear faulting (Schulson, 2004), while the sea-ice deformation multi-fractality and scaling laws are sometimes associated with the presence of a threshold/trigger, stress relaxation, and damage/healing mechanisms (Marsan & Weiss, 2010; Weiss & Dansereau, 2017; Dansereau et al., 2016).

In sea-ice dynamical models, a rheology describes the relation between the applied load and resulting deformation, effectively representing the sea-ice mechanical response to the external forcing. The Viscous-Plastic (VP) rheology with elliptical yield curve (Hibler, 1979) and its Elastic-Viscous-Plastic (EVP) variant (Hunke & Dukowicz, 1997, 2002) are the most widely used in regional and Global Climate Models (see for example Stroeve et al., 2014). In the standard VP rheology, sea ice is assumed to deform as a plastic material when the mechanical stresses reach prescribed critical loads in compression, shear, and tension (as defined by the elliptical yield curve), and as a creeping, highly-viscous fluid for smaller stresses. The EVP variant assumes the same physical concepts but uses damped artificial elastic waves that allow for an explicit numerical implementation of the dynamical equations. In this sense, the EVP approach can be considered as an alternative numerical solver for the VP rheology. Since its formulation, extensive work has been done on improving the speed and stability of the numerical schemes used for solving the (E)VP equations (e.g. Lemieux et al., 2008, 2010; Bouillon et al., 2013; Kimmritz et al., 2016), but parallel work has also pointed out inconsistencies in its basic physical assumptions (e.g. Coon et al., 2007). This has led to reconsideration of the classical (E)VP rheology by, among others, adding tensile strength (Zhang & Rothrock, 2005; König Beatty & Holland, 2010) and developing sea-ice rheologies based on different physical assumptions. Of these, the Elastic-Plastic-Anisotropic (EAP - Wilchinsky & Feltham, 2006; Tsamados et al., 2013) builds upon the artificial elastic closure of the EVP approach, but represents anisotropy of the ice stress by parameterizing the interactions of diamond-shaped floes. Long-range elastic interactions have also been explicitly included in the Elasto-Brittle (EB) and Maxwell-Elasto-Brittle (MEB) rheologies, in which the classical plastic response of the ice was traded in favor of a brittle parameterization accounting for fracturing and sliding of ice along fault planes (Girard et al., 2011; Bouillon & Rampal, 2015b; Dansereau et al., 2016).

Sea-ice models (and sea-ice rheologies) have traditionally been evaluated by estimating the error between the simulated and observed large-scale features such as sea-ice drift, thickness, concentration and extent (e.g. Flato & Hibler, 1992; Kreyscher et al., 2000; Ungermann et al., 2017). Given that these large-scale error metrics can generally be minimized by tuning the model thermodynamics, the sea-ice modeling commu-

nity has recently introduced additional metrics that specifically evaluate the small-scale deformation statistics with the goal of better discriminating/calibrating the different sea-ice rheologies. Rheology and deformation metrics are of particular interest for modelling applications requiring accurate small-scale deformation statistics (e.g. short-term drift forecasting for navigation), but also potentially for climate projections since sea-ice deformations affect ice production, vertical heat and moisture fluxes, and salt rejection to the surface ocean. Using the observed sea-ice deformation statistics has now become common practice to validate or constrain sea-ice rheologies (e.g. Girard et al., 2009; Bouillon & Rampal, 2015b; Spreen et al., 2017; Bouchat & Tremblay, 2017; Hutter et al., 2018). Specifically, the observed strain rate probability density functions (PDFs) decay exponent and the spatio-temporal scaling exponents of the total deformation rates are used as metrics to assess the ability of sea-ice rheologies and models to reproduce large deformation events and their localization and multi-fractality properties.

The application of these deformation metrics resulted in a debate about the ability of the VP sea-ice rheology to reproduce the observed deformation statistics, justifying the need for the new EB/MEB rheology (Girard et al., 2009, 2011; Rampal et al., 2016). It has since been shown that the VP rheology is able to reproduce similar deformation characteristics as the EB/MEB rheology based on the same deformation metrics (Spreen et al., 2017; Bouchat & Tremblay, 2017; Hutter et al., 2018; Hutter & Losch, 2020), leaving open the question as to whether those metrics can be used to robustly discriminate between sea-ice rheologies, and if the deformation metrics accurately capture differences in the underlying deformation statistics. Additionally, deformation fields of other sea-ice rheologies (e.g. EAP) have not been thoroughly evaluated using the new set of deformation metrics as for VP and MEB rheologies. A comprehensive assessment of the ability of different sea-ice models and rheologies to reproduce the observed deformation statistics and the sensitivity of the deformation metrics to model parameterizations was therefore identified by the sea-ice modeling working group at the Forum for Arctic Modeling and Observational Synthesis (FAMOS) Annual Meeting 2017 as a priority for the sea-ice modeling community.

To this end, the Sea Ice Rheology Experiment (SIREx) was devised with the goal of (1) understanding if the sea-ice deformation metrics, as currently applied, are useful to discriminate between the different sea-ice models/rheologies, and (2) determining how the representation of simulated sea-ice deformations can be improved to formulate recommendations for future model development. SIREx takes the form of a model inter-comparison project in which participating models are not constrained by the same configuration, allowing for low-level entry participation to better determine the usefulness of the deformation metrics as applied to a broad range of sea-ice models. The analysis of the runs from all participating models/groups is divided in two parts. First, and the subject of the present publication, the statistical distributions (PDFs) and scaling properties of the deformation fields are analyzed. Second, a feature-based comparison of the sea-ice deformation fields is performed using a recent LKF detection and tracking algorithm (Hutter et al., 2019) and is presented in a companion SIREx publication (Hutter et al., 2021).

In the present paper, we analyze the deformation statistics (i.e. PDFs, spatio-temporal scaling, and multi-fractality) for the different sea-ice models participating in SIREx with, for the first time in a single comparison study, the (E)VP, EAP, and MEB sea-ice rheologies. The goal of the paper is two-fold: (i) compare current state-of-the-art sea-ice models against observed sea-ice deformations to understand how different physical parameterizations and model configuration can impact the simulated deformation statistics, and (ii) evaluate the usefulness of the current deformation metrics to discriminate sea-ice models based on their deformation statistics and formulate more appropriate metrics if found necessary.

The paper is organized as follows. The model specifications and observations used in this study are presented in Section 2. The methods used to obtain the simulated and observed deformation fields, as well as the deformation statistics and metrics used for comparison are detailed in Section 3. Results are presented in Section 4, followed by a discussion and recommendations for model development in Section 5. Finally, a summary and concluding remarks are presented in Section 6.

2 Models and Observations

A total of 35 simulations from 11 different models contributed to the first part of SIREx. The participating models were not constrained to use the same forcing and they also vary in their spatial and temporal resolution, grid type (e.g. Eulerian vs. Lagrangian), physical parameterizations, numerical convergence criterion, etc. Specifically, only daily sea-ice velocity, thickness, and concentration fields for January-February-March of 1997 and 2008 were requested from all participating models. These two periods were chosen to allow for low-level entry participation to the study, as well as to sample different ice dynamic conditions (i.e. pre- and post- 2000's). Some groups provided two runs differing only by one component, allowing us to isolate the effects of that component on the deformation statistics. In the following, we analyze the effects of sea ice rheology jointly with spatial resolution (section 4.1), ice strength (section 4.2.1), ice thickness distribution parameterization (section 4.2.2), and atmospheric forcing (section 4.2.3). A list of all simulations and key sensitivity parameters are given in Table 1. Note that the FESOM-2 model participating in SIREx Part II does not participate in the analysis of Part I. For more information about the models, the reader can refer to the respective references in Table 1.

All participating models provided daily output on an Eulerian grid, except for neXtSIM where the output were given as Lagrangian trajectories. While spatial scaling can be studied using either Eulerian or Lagrangian deformation fields, temporal scaling requires the deformation history of tracked elements and therefore needs to be performed in a Lagrangian framework. We therefore construct Lagrangian deformation fields from the Eulerian model output before assessing the deformation statistics (see details in Section 3.2). Note that most model output were provided as daily means, but some groups provided daily snapshots. We have verified (not shown) that the Lagrangian deformation statistics presented below are robust to the choice of temporal averaging of the model output (i.e. snapshots or daily means).

The simulated deformation statistics are compared with those derived from the RADARSAT Geophysical Processor System (RGPS) Lagrangian motion data set. The RGPS Lagrangian motion data set is given as a list of trajectories (time and position) for a $10 \text{ km} \times 10 \text{ km}$ grid that is initialized at the beginning of the winter season over the central Arctic Ocean for different satellite passes (i.e. streams), tracked using sequential synthetic aperture radar (SAR) images (Kwok, 1998). The nominal spatio-temporal resolution of the RGPS Lagrangian data set is $T^* = 3$ days and $L^* = 10 \text{ km}$, however sampling of the RGPS Lagrangian data set is non-uniform given that trajectories are not always updated on the same days or at the same times or can be missing if the tracking on the SAR images was unsuccessful. For this reason, a pre-processing of the trajectories (see Section 3.1) is necessary to eliminate temporal inconsistencies that can affect the resulting sea-ice deformation statistics (e.g. Bouchat & Tremblay, 2020).

3 Methods

3.1 Pre-Processing of RGPS Lagrangian Trajectories

To ensure temporal consistency of the RGPS deformation field, we use the *Weighted-Average* pre-processing method (Hutter et al., 2019; Bouchat & Tremblay, 2020), which

Table 1. Key parameters of runs participating in SIREx. We use the following abbreviations: grid types are E: Eulerian, L:Lagrangian, U: Unstructured; Ice strength parameters are P^* : compressive strength parameter (kPa), T^* : isotropic tensile strength parameter (kPa), e : ellipse aspect ratio, C_f : frictional energy dissipation parameter; ITD # is the number of ice-thickness categories in the ice thickness distribution; and *(solver/nb. it)* is the numerical solver used to solve the VP momentum equations or the number of elastic iterations performed to solve the EVP/EAP equations. The grid spacing is given by the mean horizontal grid spacing within the Arctic Ocean. For unstructured grids it refers to the mean node spacing.

| Model/Configuration (Group) Label | Year | Grid spacing, Time step | Grid | Rheology (solver/nb. it) | Ice Strength Parameters | ITD # | Atm. Forcing (Δx , Δt) | Reference |
|---|------------|----------------------------|------|-----------------------------|---|----------|--|--------------------------------|
| MITgcm | | | | | | | | |
| (AWI) | | | | | | | | |
| MITgcm (2km, ITD) | 2008 | 2 km, 120s | E | VP (LSR) | P^* , $e = 22.64$, 2.0 | 5 | JRA55 (~60 km, 3 hr) | (Hutter & Losch, 2020) |
| MITgcm (2km, $e=1, \downarrow P$) | 1997, 2008 | " | " | " | P^* , $e = 9.6$, 1.0 | 2 | " | - |
| MITgcm (2km, $e=0.7, \downarrow P$) | 1997, 2008 | " | " | " | P^* , $e = 9.6$, 0.7 | " | " | - |
| MITgcm (2km) | 1997, 2008 | " | " | " | P^* , $e = 22.64$, 2.0 | " | " | (Hutter & Losch, 2020) |
| MITgcm (4.5km) | 2008 | 4.5 km, 240s | " | " | " | " | ERA-Interim (~80 km, 6 hr) | (Mohammadi-Aragh et al., 2018) |
| McGill-SIM | | | | | | | | |
| (McGill) | | | | | | | | |
| McGill (e=2) | 1997 | 10 km, 3600s | E | VP (JFNK) | P^* , $e = 27.5$, 2.0 | 2 | NCEP/NCAR (2.5°, 6 hr) | (Bouchat & Tremblay, 2017) |
| McGill (e=1, $\downarrow P$) | 1997 | " | " | " | P^* , $e = 13.8$, 1.0 | " | " | " |
| McGill (e=0.7, $\downarrow P$) | 1997 | " | " | " | P^* , $e = 9.6$, 0.7 | " | " | " |
| McGill (e=1, $\uparrow S$) | 1997 | " | " | " | P^* , $e = 27.5$, 1.0 | " | " | " |
| NEMO-LIM3/CREG4 | | | | | | | | |
| (IFREMER) | | | | | | | | |
| IFREMER (e=2) | 1997, 2008 | 12.4 km, 720s | E | EVP (120) | P^* , $e = 20.0$, 2.0 | 5 | DFS 5.2 (~0.7°, 3 hr) | (Muitwijk et al., 2019) |
| IFREMER (e=1) | 1997, 2008 | " | " | " | P^* , $e = 13.8$, 1.0 | " | " | " |
| HYCOM-CICE4 | | | | | | | | |
| (FSU) | | | | | | | | |
| HYCOM-CICE (FSU) | 1997, 2008 | 3.6 km, 360s | E | EVP (120) | $C_f, e = 19, 2.0$ | 5 | CFSR/CFSv2 (~38 km, 1 hr) | (Dukhovskoy et al., 2019) |
| HYCOM-CICE4 | | | | | | | | |
| (DMI) | | | | | | | | |
| 2008 | 2008 | 9.7 km, 180s | E | EVP (120) | P^* , $e = 27.5$, 2.0 | 5 | ERA-Interim (80 km, 3 hr) | (Madsen et al., 2016) |
| MERCATOR/CREG12 | | | | | | | | |
| (Mercator Ocean) | | | | | | | | |
| 1997, 2008 | 1997, 2008 | 4.1 km, 900s | E | EVP (500) | P^* , $e = 27.5$, 1.5 $T^* = 1.375$ | 5 | ERA-Interim (80 km, 3 hr) | (Dupont et al., 2015) |
| NEMO-LIM2/ANHA12 | | | | | | | | |
| (U. Alberta) | | | | | | | | |
| 2008 | 2008 | 4.1 km, 180s | E | EVP (120) | P^* , $e = 23.4$, 2.0 | 2 | CGRF (~35 km, 1 hr) | (Hu et al., 2018) |
| NEMO-LIM2/ANHA4 | | | | | | | | |
| (U. Alberta) | | | | | | | | |
| 1997, 2008 | 1997, 2008 | 12.4 km, 1080s | E | EVP (150) | P^* , $e = 23.4$, 2.0 | 2 | CORE (~200 km, 6 hr) | (Courtois et al., 2017) |
| RIPS/CREG12-H08 | | | | | | | | |
| (BCCC) | | | | | | | | |
| 2008 | 2008 | 4.1 km, 180s | E | EVP (900) | P^* , $e = 27.5$, 1.5 $T^* = 1.375$ | 10 | CGRF (~35 km, 3 hr) | (Dupont et al., 2015) |
| FESOM | | | | | | | | |
| (AWI) | | | | | | | | |
| 1997, 2008 | 1997, 2008 | 5.1 km, 600s | U | EVP (800) | P^* , $e = 27.5$, 2.0 | 2 | NCEP/NCAR (~1.9°, 24 hr) | (Wang et al., 2016) |
| RASM - Fully Coupled | | | | | | | | |
| (NPS) | | | | | | | | |
| 1997, 2008 | 1997, 2008 | 9.1 km, 1200s | E | EVP (600) | $C_f, e = 21.3$, 2.0 | 5 | WRF Model (50 km, 20 min) | - |
| RASM-CORE2 | | | | | | | | |
| (NPS) | | | | | | | | |
| 1997, 2008 | 1997, 2008 | 9.1 km, 1200s | E | EAP (600) | " | " | " | - |
| neXtSIM - V1(2018) | | | | | | | | |
| (NERSC) | | | | | | | | |
| 1997, 2008 | 1997, 2008 | 9.1 km, 1200s | E | EAP (120) | $C_f, e = 21.3$, 2.0 | 5 | CORE2 (~110 km, 24 hr) | - |
| neXtSIM | | | | | | | | |
| (Rampal et al., 2019) | | | | | | | | |
| 1997, 2008 | 1997, 2008 | 10 km, 200s | L | MEB | $T^*, P^* = 21$, 75 | 3 | CFSR/CFSv2 (0.5° version, 6 hr) | (Rampal et al., 2019) |

consists in keeping only trajectories forming cells that have (i) simultaneous (± 3 hours) start and end times for all four corners, (ii) an average time resolution for all corners that corresponds to the nominal temporal resolution of $T^* = 3$ days, and (iii) an area corresponding to the nominal spatial resolution of $L^* = 10$ km. We also require that all corner positions remain at least 100 km away from land for the present analysis. The remaining trajectories are then used to compute the Lagrangian strain rates (see e.g. Equations 1–5 below) and the resulting time series of strain rates for each cell are then averaged in regular 3-day intervals (using a weighted-average of contributing strain rate estimates) starting on January 1st each year. For more information on the pre-processing of the RGPS Lagrangian trajectories and the resulting observed strain rate data set, we refer the reader to Bouchat and Tremblay (2020).

3.2 Constructing Simulated Lagrangian Trajectories and Deformation Fields

To construct simulated Lagrangian trajectories and deformation fields from Eulerian model output, we track artificial Lagrangian quadrangle cells that are initialized with the 10-km RGPS Lagrangian positions on 1 January 1997 and 2008. Model trajectories are integrated in their respective grid projection using 1-hour time increments to prevent trajectories from crossing multiple grid cells during one integration step. At the beginning of each hour, the daily mean or snapshot sea-ice velocity field (u, v) is first linearly interpolated in time to the current integration time, and then spatially interpolated onto the trajectories' positions using a Great-Circle distance-weighted linear interpolation of the four nearest velocity components (e.g. Madec, G. and NEMO System Team, 2019). Trajectories are integrated until March 31, unless they drift to within 100 km of the model landmask in which case they are terminated. When the Lagrangian integration is done, the hourly model trajectories are sampled at the beginning of the same regular 3-day intervals as for the RGPS *Weighted-Average* data set. In the case of data gap in the RGPS data set, we remove the corresponding simulated trajectory to minimize the effects of the different spatio-temporal coverage on the deformation statistics. Note that the initialization of the model trajectories with RGPS positions and the 3-day temporal sampling ensure that the nominal spatial and temporal resolutions of the simulated Lagrangian deformation fields are the same as for the RGPS observations (i.e. $L^* = 10$ km and $T^* = 3$ days), regardless of the original resolution of the model.

The strain rates (velocity gradients) and cell area A are then computed for each cell using the line integral approximations (e.g. Lindsay & Stern, 2003):

$$\frac{\partial u}{\partial x} = \frac{1}{A} \sum_{k=1}^4 \frac{1}{2} (u_{k+1} + u_k) (y_{k+1} - y_k) , \quad (1)$$

$$\frac{\partial u}{\partial y} = \frac{-1}{A} \sum_{k=1}^4 \frac{1}{2} (u_{k+1} + u_k) (x_{k+1} - x_k) , \quad (2)$$

$$\frac{\partial v}{\partial x} = \frac{1}{A} \sum_{k=1}^4 \frac{1}{2} (v_{k+1} + v_k) (y_{k+1} - y_k) , \quad (3)$$

$$\frac{\partial v}{\partial y} = \frac{-1}{A} \sum_{k=1}^4 \frac{1}{2} (v_{k+1} + v_k) (x_{k+1} - x_k) , \quad (4)$$

with,

$$A = \frac{1}{2} \sum_{k=1}^4 (x_k y_{k+1} - x_{k+1} y_k) , \quad (5)$$

where (x_k, y_k) is the position of the cell vertex k at time t ($k = 1, 2, 3, 4$; counterclockwise with $x_5 = x_1$ and similar cyclical identities for y_5, u_5 , and v_5) and $(u_k, v_k) = (\frac{\Delta x_k}{\Delta t}, \frac{\Delta y_k}{\Delta t})$,

their approximate velocity during the time interval Δt . The spatial scale of the strain rate estimate is $L = \sqrt{A}$, and its temporal scale is $T = \Delta t = T^* = 3$ days. Following Bouchat and Tremblay (2020), all cells where $A \leq 50$, or $A \geq 200 \text{ km}^2$ are removed in order to only keep cells that are representative of the nominal spatial scale ($L^* = 10 \text{ km}$).

The strain rate invariants (ie. divergence $\dot{\epsilon}_I$, and shear $\dot{\epsilon}_{II}$) and total deformation rates ($\dot{\epsilon}_{tot}$) are obtained as:

$$\dot{\epsilon}_I = \frac{\partial u}{\partial x} + \frac{\partial v}{\partial y}, \quad (6)$$

$$\dot{\epsilon}_{II} = \left[\left(\frac{\partial u}{\partial x} - \frac{\partial v}{\partial y} \right)^2 + \left(\frac{\partial u}{\partial y} + \frac{\partial v}{\partial x} \right)^2 \right]^{1/2}, \quad (7)$$

$$\dot{\epsilon}_{tot} = \sqrt{\dot{\epsilon}_I^2 + \dot{\epsilon}_{II}^2}. \quad (8)$$

3.3 Deformation Statistics and Associated Metrics

We detail below the deformation statistics used in this study (i.e. probability density functions of shear and absolute divergence, spatio-temporal scaling of the mean total deformation rates, and multi-fractal scaling analysis) along with their usual comparison metrics.

3.3.1 Probability density functions (PDFs)

PDFs for the shear and absolute divergence are used to evaluate the ability of sea-ice models to reproduce large deformation rates and to characterize their statistical distribution. The observed RGPS PDFs of strain rate invariants are heavy-tailed and decay approximately linearly in log-log plots (e.g. Girard et al., 2009, 2011; Bouillon & Rampal, 2015b; Bouchat & Tremblay, 2017; Rampal et al., 2019).

Here, the PDFs are obtained using logarithmic bins and the typical metric used to compare the observed and simulated PDFs is the decay exponent of the tail, obtained as the slope of a least-square linear fit in log-log space. We do not fix the fitting interval, but rather use an interval of one order of magnitude ending on the largest deformation bin available (or use the maximum available fitting interval if the PDFs spans less than one order of magnitude). We do this because models do not necessarily reproduce deformation rates as large as in the RGPS distributions. Note that it has recently been shown that a power-law distribution is not a suitable hypothesis for the observed RGPS PDFs based on a goodness-of-fit test (Bouchat & Tremblay, 2020). We therefore consider that a linear fit is sufficient to obtain an estimate of the decay exponent (e.g. as opposed to using the more robust Maximum Likelihood Estimator) until a better description of the observed deformation distribution is known.

3.3.2 Spatio-temporal scaling analysis of the mean total deformation rates

We use the coarse-graining procedure with data-quality weights described in Bouchat and Tremblay (2020) to generate deformation fields at larger scales and investigate the spatial and temporal scaling of the mean total deformation rates, i.e.:

$$\langle \dot{\epsilon}_{tot}(L, T) \rangle \sim L^{-\beta}, \quad (9)$$

$$\langle \dot{\epsilon}_{tot}(L, T) \rangle \sim T^{-\alpha}, \quad (10)$$

where $\langle \cdot \rangle$ denotes the distribution weighted average, L and T are the spatial and temporal scales of the coarse-grained deformation estimates, and β and α are the spatial and temporal scaling exponents.

The values of β and α characterize the degree of spatial and temporal localization of the mean total deformation rates, and are used as metrics to compare the observed and simulated spatio-temporal scaling. The spatial scaling exponent β varies between 0 (deformation field is homogeneous in space) and 2 (deformations are highly localized in space), while the temporal scaling exponent α varies between 0 (deformations field is homogeneous in time) and 1 (deformations are highly localized in time). Here, β and α are obtained using least-square power-law fits on the average total deformation rates $\langle \dot{\epsilon}_{tot}(L, T) \rangle$ for a given range of spatial and temporal scales. We restrict the spatial scaling to scales $10 \leq L \leq 600$ km and the temporal scaling to scales $3 \leq T \leq 30$ days to minimize the effects of the reduced spatio-temporal coverage at larger scales.

Using data-quality weights to obtain the distribution average at each scale results in giving more weight to the tail of the distribution where interesting sea-ice dynamical features are represented (e.g., LKFs) and where deformation rates have smaller relative errors. As discussed in Section 4.1.2, this improves the interpretation of the scaling exponent metrics as a measure of localization of deformations when applied to simulated deformation fields. The data quality is defined by the signal-to-noise ratios which are obtained by estimating the Lagrangian trajectory errors. The details of the signal-to-noise ratio calculations for RGPS and simulated Lagrangian trajectories can be found in Appendix A.

3.3.3 Multi-fractal analysis

The spatio-temporal scaling analysis described for the mean total deformation rate above is repeated for higher moments q to construct $\beta(q)$ and $\alpha(q)$, the spatial and temporal structure functions, i.e.:

$$\langle \dot{\epsilon}_{tot}^q(L, T) \rangle \sim L^{-\beta(q)}, \quad (11)$$

$$\langle \dot{\epsilon}_{tot}^q(L, T) \rangle \sim T^{-\alpha(q)}. \quad (12)$$

It has usually been assumed that the structure functions $\beta(q)$ and $\alpha(q)$ for sea-ice total deformation rates are quadratic, e.g. $\beta(q) = aq^2 + bq$, where a has been interpreted as the degree of multi-fractality of the scaling (e.g. Bouillon & Rampal, 2015b; Hutter et al., 2018; Rampal et al., 2019; Bouchat & Tremblay, 2020). However, following the universal multi-fractal formalism, the structure functions are not required to be quadratic and can have a varying degree of non-linearity, which is then more correctly interpreted as the degree of multi-fractality (Lovejoy & Schertzer, 2007, 2013). Here, we do not assume a fixed degree of multi-fractality and instead find a general least-square fit for the structure functions of the following form (in full agreement with the universal multi-fractal formalism — e.g. Lovejoy & Schertzer, 1995, 2007; Weiss, 2008):

$$\beta(q) = q - \zeta(q), \quad (13)$$

with,

$$\zeta(q) = qH - K(q), \quad (14)$$

and

$$K(q) = \frac{C_1}{\mu - 1} (q^\mu - q), \quad (15)$$

such that we can write:

$$\beta(q) = \left(\frac{C_1}{\mu - 1} \right) q^\mu + \left(1 - \left(H + \frac{C_1}{\mu - 1} \right) \right) q, \quad (16)$$

where H is a fluctuation exponent, $K(q)$ is the universal multi-fractal moment scaling function, C_1 ($0 \leq C_1 \leq 2$) characterizes the degree of heterogeneity (or sparseness) of the field, and μ ($0 \leq \mu \leq 2$) is the degree of multi-fractality ($\mu = 0$ for a mono-fractal process, and $\mu = 2$ for a log-normal multiplicative model with maximal degree of multi-fractality). An equivalent formulation applies for the temporal structure function $\alpha(q)$.

In the following, the values of the three multi-fractal parameters H , C_1 , μ are used as metrics to compare the observed and simulated multi-fractal structure functions.

4 Results

Results for low-resolution model runs ($\Delta x = 9\text{--}12\text{ km}$) are presented separately from high-resolution model runs ($\Delta x = 2\text{--}5\text{ km}$), even if their Lagrangian deformation fields are reconstructed at the same nominal spatial scale of $L^* = 10\text{ km}$. In fact, Eulerian models with finite-difference schemes will resolve the sea-ice dynamics with different levels of complexity as their spatial resolution changes (e.g. Spreen et al., 2017; Williams & Tremblay, 2018). It is therefore expected that higher resolution runs will resolve finer deformation features in their Lagrangian deformation fields, affecting the result of the deformation metrics. For instance, consider the observed sea-ice deformation field sampled at $L^*=10\text{ km}$. The deformation statistics at this scale are the result of underlying dynamics occurring at much finer scales (e.g. fractures at the sub-km scales). The observed deformation fields sampled at $L^*=10\text{ km}$ are therefore much more rich in information than model deformation fields that are generated (rather than sampled) at the same nominal spatial scale, unless sub-grid parameterization are used and calibrated. Degrading the observed deformation fields to larger spatial scales could help minimizing this discrepancy when comparing the observed and simulated deformation statistics, but only if the degraded spatial scales are much larger than the nominal spatial scales at which models are run (e.g. observations at $L \sim 50 - 100\text{ km}$ vs. models at $L \sim 10\text{ km}$), in which case the range of scales available for determining the observed statistical characteristics (e.g. spatio-temporal localization) becomes too small. Note that we also consider atmosphere-ice-ocean coupled model simulations (with forcing fields at much higher spatio-temporal resolution) separately from coupled ice-ocean models (or stand-alone ice models) forced with reanalyses (see Section 4.2.3).

In the following sections, the agreement between models and observations is interpreted in terms of the RGPS interannual variability. That is, metrics are first obtained for all years in the RGPS record and, unless stated otherwise, the full RGPS distribution is used as a range defining a good agreement between models and observations.

4.1 Effects of sea-ice rheology

4.1.1 Probability Density Functions

Most of the simulated PDFs of shear and absolute divergence decay approximately linearly in log-log plot, with a wide range of simulated decay exponents (Figures 1–4, top panels). We note that very different distributions can lead to very similar decay exponents, suggesting that this metric does not adequately capture differences in the deformation fields (for example, compare RGPS with HYCOM-CICE (FSU) in Figure 3, or with IFREMER (e=1) in Figure 2). We therefore define a new metric as the sum of the absolute difference between the simulated and observed PDFs in logarithmic scale, divided by the number of bins spanned by the simulated PDF. Dividing by the number of bins ensures that the metric penalizes models that do not simulate sufficiently large deformation rates and have a smaller number of bins. An advantage of this metric is that differences in the tail of the PDFs (i.e. where probabilities are small, but represent larger deformation rates that are likely to affect climate interactions or operational applications)

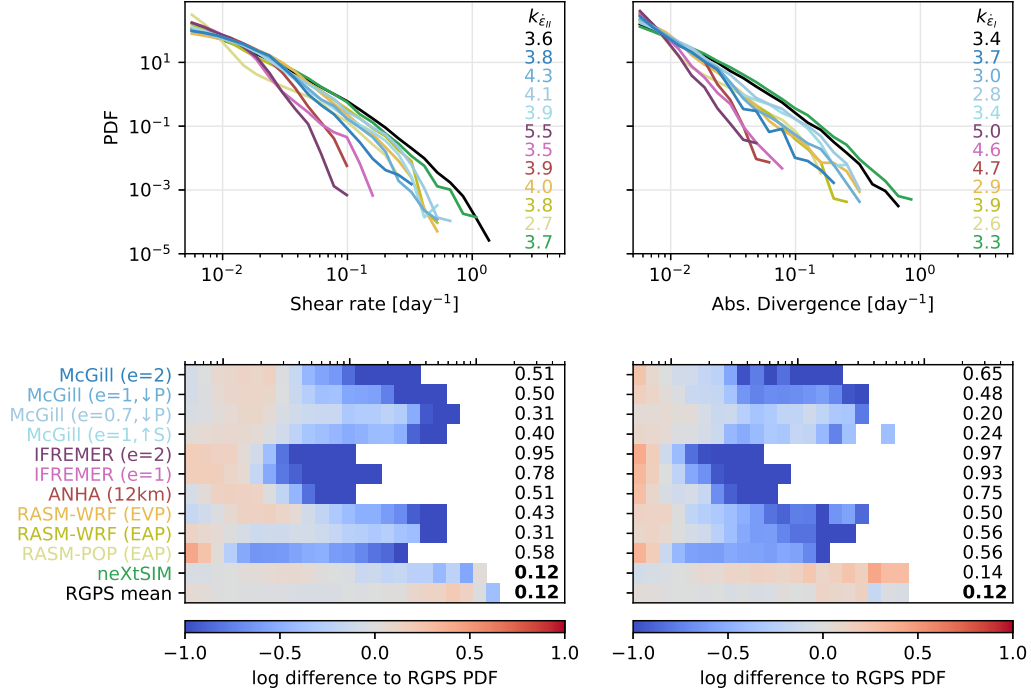


Figure 1. Top: Probability density functions (PDFs) of maximum shear rate (left) and absolute divergence (right), for low-resolution runs ($\Delta x \simeq 10$ km) and RGPS observations (black) at $L=10$ km and $T=3$ days in January-February-March 1997. Each run is identified in the lower-left panel by a different color corresponding to its sea-ice rheology (Blue/Purple: VP, Pink/Red: EVP, Yellow: EAP, Green: MEB) and insets give the decay exponents $k_{\dot{\epsilon}_{II}}$ and $k_{\dot{\epsilon}_I}$; Bottom: Difference (per bin) between the logarithm of models and RGPS PDFs. The insets give the average absolute difference per bin, where bold font marks values that are equal to or less than the RGPS interannual average obtained using all other RGPS years in comparison to 1997.

are given more weight by using a logarithmic scale. To interpret the value of the metric, we compute its interannual variability for all available RGPS observations, using either the RGPS PDFs of 1997 or 2008 as the reference and computing the difference metric with all other years in the RGPS data set. We then use the mean value of the RGPS PDFs difference metric for each comparison year (one value for 1997 and another for 2008) as an upper threshold defining a reasonable agreement between models and observations. These reference mean values, as well as the mean difference per bin (in logarithmic scale) for the RGPS data set are shown in Figures 1–4 (bottom panels) for comparison.

Out of all low-resolution runs, we find that only the neXtSIM simulations show an agreement with the observed PDFs (Figures 1–2, bottom panels). This reflects a clear underestimation of the range over which the PDFs extend (i.e. smaller number of bins), along with a drop in probabilities in the respective last bins of the PDFs for low-resolution runs with plastic rheologies ((E)VP, EAP). Only the neXtSIM model (MEB) captures deformations in the largest observed bins at low-resolution. Modifying the plastic elliptical yield curve parameters at low resolution helps increasing the range over which the PDFs extend and also reduces the drop in the tail, especially in divergence (see also Section 4.2.1).

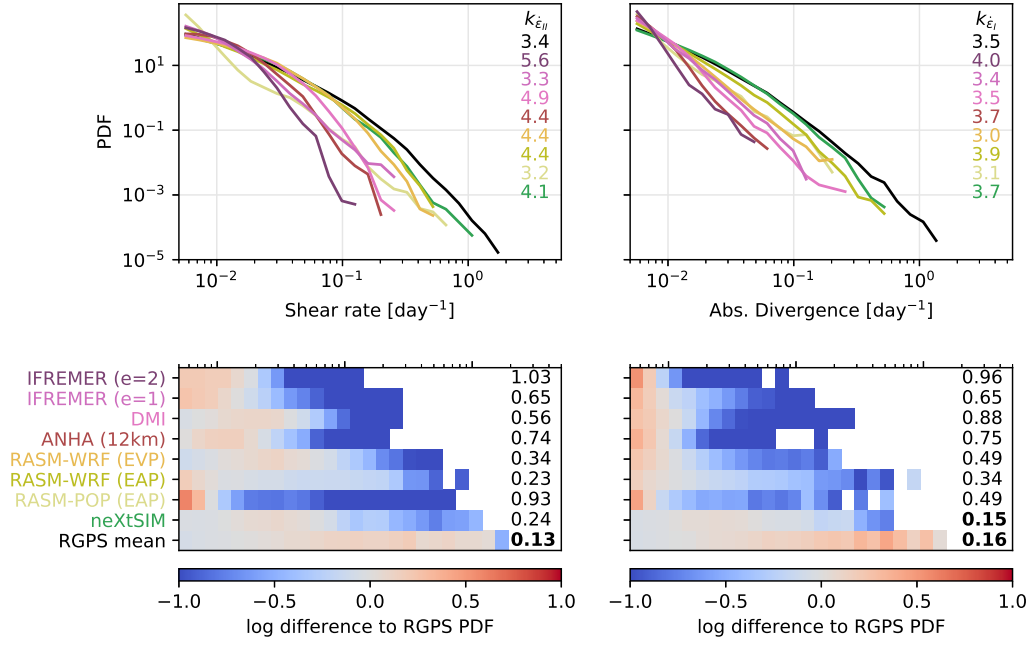


Figure 2. Same as Figure 1 for low-resolution runs ($\Delta x \approx 10$ km) in January-February-March 2008.

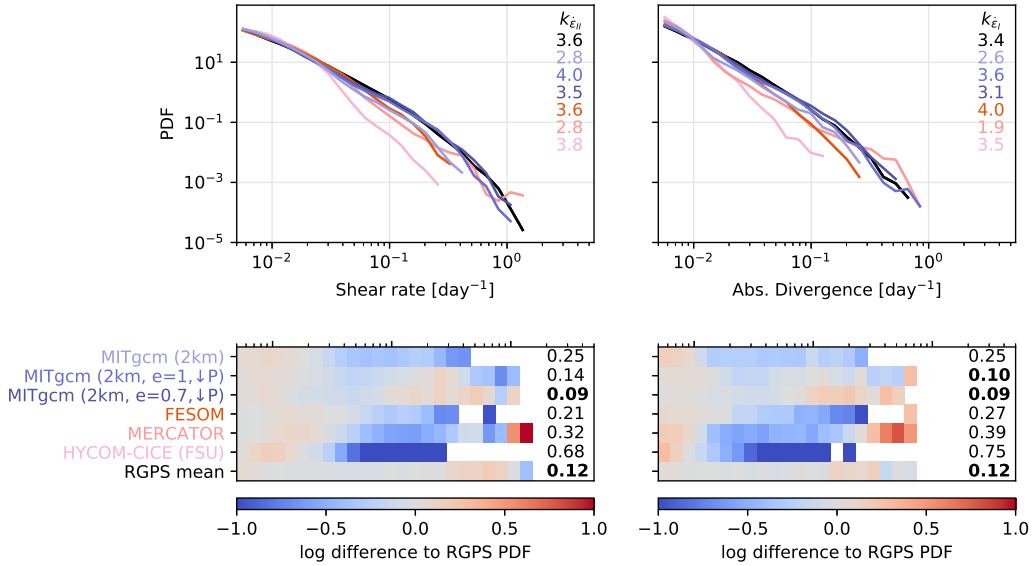


Figure 3. Same as Figure 1 for high-resolution runs ($\Delta x \approx 2-5$ km) in January-February-March 1997.

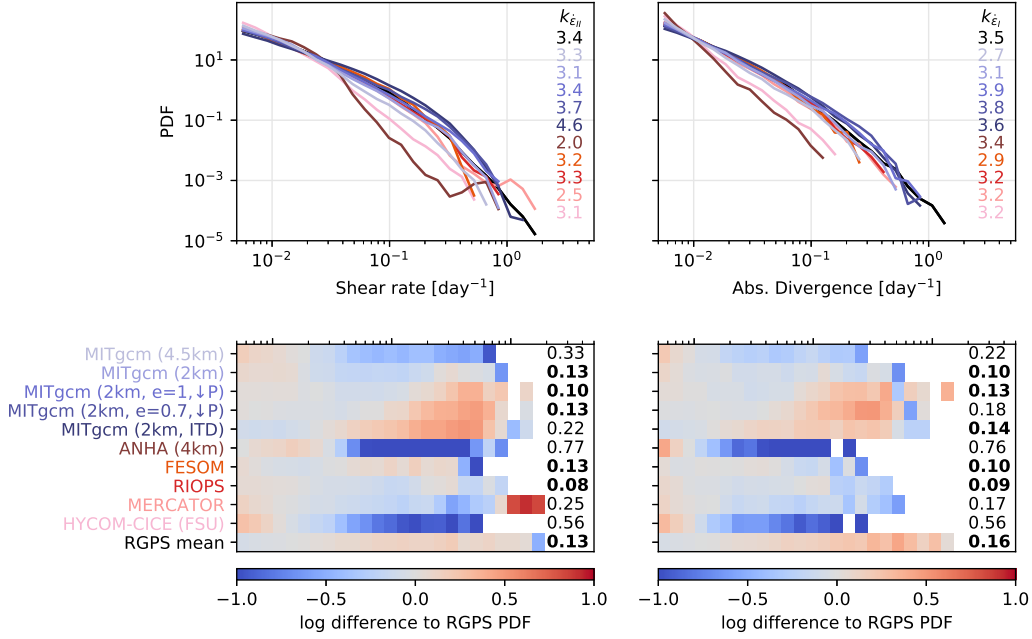


Figure 4. Same as Figure 1 for high-resolution runs ($\Delta x \simeq 2\text{--}5$ km) in January–February–March 2008.

Increasing the spatial resolution of the models generally improves the agreement of simulated PDFs with observations (Figures 3–4). This can be attributed in part to a refinement of LKFs in which deformation rates increase at higher resolution (e.g. Spreen et al., 2017; Williams & Tremblay, 2018), and in part to an increased spatio-temporal LKF density (Hutter et al., 2021). We find that high-resolution runs with the (E)VP rheology (i.e. the only rheology represented by the very-high resolution runs) can reproduce PDFs that agree reasonably well with the RGPS shear and absolute divergence simultaneously. However, some EVP runs at high-resolution still poorly agree with the RGPS PDFs, even if the range of the simulated PDFs is improved compared to low-resolution EVP runs (see e.g. HYCOM-CICE (FSU) and ANHA 4km). We hypothesize that this reflects a numerical artifact originating from insufficient subcycling with the EVP approach. In the EVP equations, an artificial elastic strain is added to the VP rheology to allow explicit solving of the momentum equations. Within each advective time step, small iteration steps (subcycling) are used to explicitly advance the solution, while damping the artificial elastic waves in order to recover a solution that approximates a VP solution. When using too few subcycles with the EVP solver, the solution is noisy with large residual errors, and the probability of simulating large deformation rates is significantly reduced (Lemieux et al., 2012; Kimmritz et al., 2015). While we cannot explicitly check their numerical convergence, we note that noise is present in the EVP deformation fields analyzed here (results not shown), and that the EVP runs poorly agreeing with the observed RGPS PDF consistently use a small number of subcycles (and vice-versa: EVP runs showing a good PDF agreement also use a large number of subcycles — see e.g. ANHA 4km: 120 subcycles, vs. RIOPS: 900 subcycles in Figure 4). We therefore hypothesize that the high-resolution EVP runs showing a poor PDF performance here are also affected by large residual errors originating from undamped elastic waves and too few subcycles. This could explain the lower performance of EVP compared to VP for low-resolution runs as well, but it remains to be validated with further experiments.

4.1.2 Spatio-Temporal Scaling and Coupling

The spatio-temporal scaling analysis of simulated deformation rates has typically been investigated without using data-quality weights (Girard et al., 2009; Bouillon & Rampal, 2015a; Spreen et al., 2017; Bouchat & Tremblay, 2017; Hutter et al., 2018; Rampal et al., 2019). Considering high-resolution sea-ice simulations, Hutter and Losch (2020) showed that the spatio-temporal scaling exponents depend on the LKF density, such that a run with fewer LKFs returned lower scaling exponents. However, lower scaling exponents are also expected for diffuse deformation fields (see Section 3.3.2). We find here that the spatial scaling exponents for simulated deformation fields with few but highly-localized deformations can in fact be comparable to those for deformation fields with obviously less localized deformations when the data quality (signal-to-noise ratio) is not used to weight the deformation estimates in the scaling analysis (see example in Figure 5a). In contrast, using the signal-to-noise ratios to weight the simulated deformation distribution helps to distinguish between both cases, as the scaling exponents increase for simulations with highly-localized deformation features, while they remain low for more diffuse deformation fields (Figure 5b). This is in agreement with Bouchat and Tremblay (2020) who showed that signal-to-noise ratio weights enhance the spatio-temporal scaling exponents of RGPS observations due to the added weight in the tail of the distribution where highly-localized deformation features are prominent. Implementing the scaling analysis with signal-to-noise ratio weights to compare observations and models therefore improves the interpretation of the scaling exponent metric as a measure of the localization of the deformation fields. It also allows us to investigate the presence of a spatio-temporal coupling of the spatial and temporal scaling exponents (i.e. a logarithmic decay of β and α when increasing T and L , respectively - Marsan & Weiss, 2010), which is otherwise absent for the observed RGPS mean total deformation rates when using weights equal to one (Bouchat & Tremblay, 2020). Note that, while the coupling and scaling exponents are affected, we have verified that finding a power-law scaling in space or time does not depend on the weights used to average the deformation distribution (i.e. signal-to-noise ratio weights vs. weights equal to one as in previous studies). In the following, the scaling analysis is performed with the signal-to-noise ratio weighting method.

We find that all sea-ice rheologies produce a power-law spatial scaling of the total deformation rates holding over ~ 1.5 orders of magnitude (i.e. $10 \leq L \leq 600$ km — Figures 6–7, a and b). However, the simulated spatial scaling exponent β (i.e. the slope of the power-law decay in log-log space) varies largely from run to run (Figures 6–7, c and d). We note that the only runs showing a spatial scaling exponent large enough to be within the observed RGPS interannual variability (or larger) also showed a reasonable agreement in their PDFs of deformations (i.e. neXtSIM, RIOPS, FESOM, and MIT-gcm - 2km). The presence of large deformation rates therefore appears as a necessary condition for also having a large degree of spatial localization. It is not sufficient however, since it is the spatial organization of these large deformation rates along well-defined features (i.e. LKFs) that is responsible for the spatial scaling (e.g. Marsan et al., 2004; Stern & Lindsay, 2009).

For low-resolution runs, the largest spatial scaling exponents are obtained with the MEB rheology (neXtSIM). While the neXtSIM deformation fields do show highly localized LKFs (Figure 8), this model uses an adaptive Lagrangian mesh as opposed to a static Eulerian grid as in all other runs. It is therefore not straightforward to attribute this stronger spatial localization of deformation to the rheology alone since moving meshes are known to be very efficient at capturing and preserving singularities or discontinuities in the solution (e.g. Cenicerros & Hou, 2001).

The lowest spatial scaling exponents are obtained with the EVP rheology, in both low- and high-resolution runs (Figures 6–7, c and d). The deformation fields for these runs (i.e. DMI, IFREMER, HYCOM-CICE (FSU), ANHA 4km and 12km) clearly underestimate the presence of well-defined deformation features (Figures 8–9 and Hutter

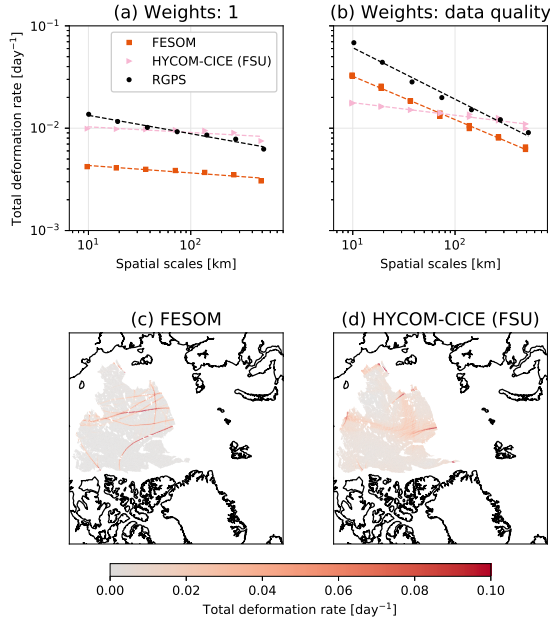


Figure 5. Example of spatial scaling for total deformation rates estimated at $T = 3$ days in January-February-March 1997 using weights equal to one (a), and weights equal to the signal-to-noise ratios of the deformation estimates (b), for two high-resolution runs showing distinctly localized total deformation fields (c and d — snapshot examples for January 28-30 1997, in day⁻¹).

et al., 2021). We again hypothesize that this could be due to insufficient damping of the artificial elastic wave and small numbers of subcycling steps, but the effects of the numerical convergence on the scaling statistics need to be further evaluated. We note, however, that more iterations to obtain more accurate VP and EVP solutions leads to additional lines of deformations in the solution (Lemieux et al., 2012; Bouchat & Tremblay, 2014; Wang et al., 2016; Koldunov et al., 2019), which should increase the spatial scaling exponent (or spatial localization).

Ignoring the runs with a smaller number of subcycles mentioned above, the spatial scaling exponent for (E)VP runs generally increases as the grid is refined. This is consistent with a refinement of the spatial localization of deformation lines with increasing spatial resolution in Eulerian plastic sea-ice models (Williams & Tremblay, 2018). In contrast, the spatial scaling exponent was shown to be approximately resolution-independent for neXtSIM (MEB) when tested on a range of spatial resolutions from 30 to 7.5 km (Rampal et al., 2019). It is still unclear whether this is a consequence of using a Lagrangian mesh that better adapts to discontinuities in the solution (regardless of the resolution), or of using a brittle rheology. We can however conclude that a large spatial localization of deformation is possible for both visco-plastic ((E)VP) and brittle visco-elastic (MEB) rheologies, as long as Eulerian sea-ice models are run at high spatial resolution. Modifying the ice strength parameters and the atmospheric forcing also has a large effect on increasing the scaling exponents as discussed later in Sections 4.2.1 and 4.2.3.

Interestingly, both low- and high-resolution runs span a similar range of temporal scaling exponents that overlaps with the RGPS interannual variability, showing that a strong degree of temporal localization of deformations is reproduced by all models, at least for the range of temporal scales considered in this study (i.e. [3–30] days — Fig-

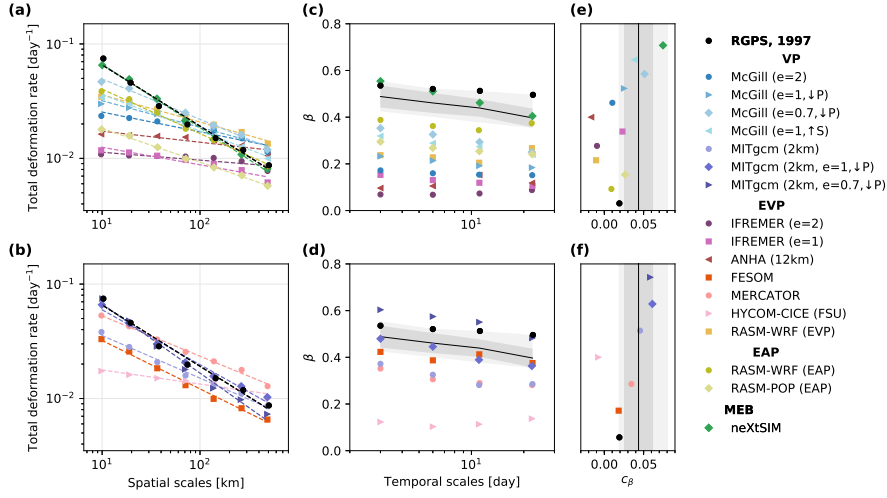


Figure 6. (a,b): Spatial scaling for total deformation rates estimated at $T = 3$ days in January-February-March 1997. (c,d): Spatial scaling exponent β as a function of the temporal scale T at which the mean total deformation rates are estimated. (e,f): Coupling coefficient c_β obtained from least-squares logarithmic fits $\beta \sim c_\beta \ln(T)$ for $3 \leq T \leq 30$ days. Dashed lines are the least-square power-law fits used to obtain β . The solid black lines, dark gray, and light gray shaded areas are the mean, standard deviation, and min/max for the entire RGPS data set. Model results are separated with low-resolution runs in top panels, and high-resolution runs in bottom panels.

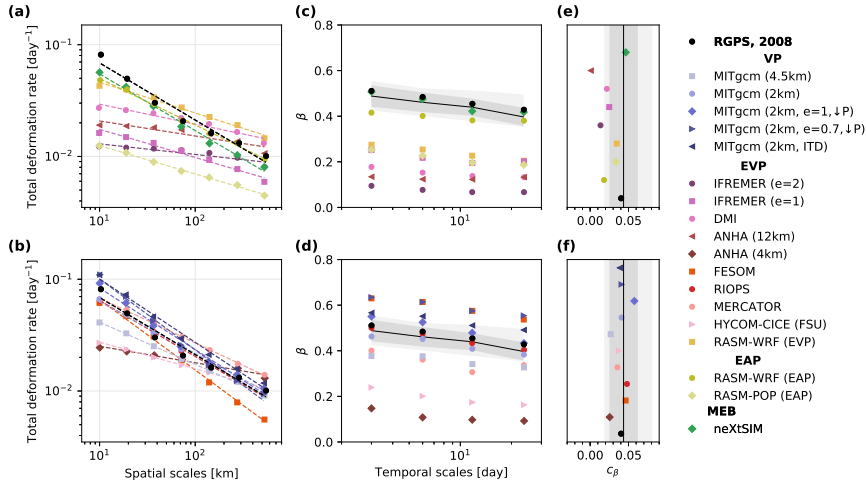


Figure 7. Same as Figure 6 for total deformation rates in January-February-March 2008.



Figure 8. Total deformation rate snapshots (in day^{-1}) for selected runs for the period of 21-22-23 February 2008.



Figure 9. Total deformation rate snapshots (in day^{-1}) for selected runs for the period of 10-11-12 January 1997.

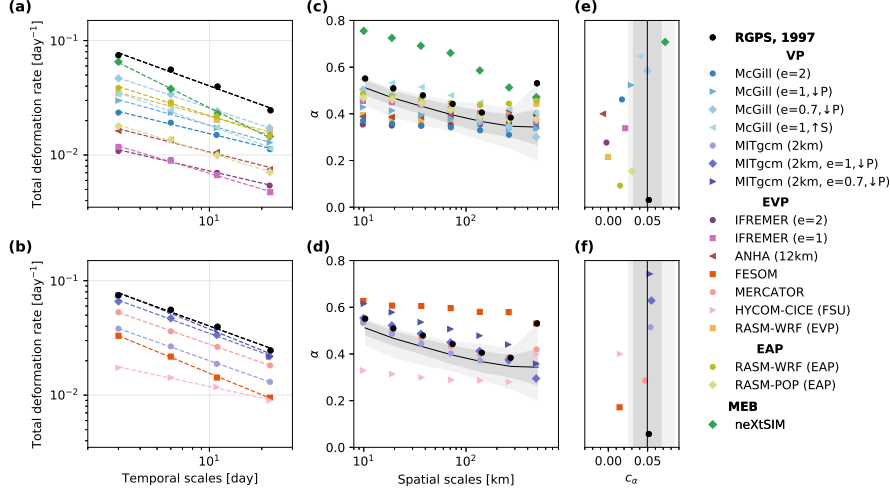


Figure 10. (a,b): Temporal scaling for total deformation rates estimated at $L=10$ km in January-February-March 1997. (c,d): Temporal scaling exponent α as a function of the spatial scale L at which the mean total deformation rates are estimated. (e,f): Coupling coefficient c_α obtained from least-squares logarithmic fits $\alpha \sim c_\alpha \ln(L)$ for $10 \leq L \leq 300$ km. Dashed lines are the least-square power-law fits used to obtain α . The solid black lines, dark gray, and light gray shaded areas are the mean, standard deviation, and min/max for the entire RGPS data set. Model results are separated with low-resolution runs in top panels, and high-resolution runs in bottom panels.

ures 10 and 11). Here, it is important not to confuse strong temporal localization with strong intermittency. A field can be highly localized in time, but it is the change of localization within the data set (or with changing deformation magnitude) that reflects the intermittency (or heterogeneity). The intermittency of the deformation field is indicated by its (non-linear) moment scaling function (or *structure function*) which is investigated in Section 4.1.3. Temporal scaling (or localization in time) of the deformation rates is assumed to originate from the presence of long-ranged temporal correlations in the time series of deformations. We have verified that when randomly re-ordering the times series of deformation, the power-law temporal scaling is lost for both RGPS observations and simulated deformation fields (results not shown). This is analogous to the presence of long-ranged spatial correlation (for instance, LKFs) giving rise to the spatial scaling. The origin of these temporal correlations in models and observations remains to be identified. We note however that a larger simulated temporal scaling exponent does not necessarily correlate with the use of a smaller advective time-step, nor with higher spatio-temporal resolution of the atmospheric forcing. Preliminary analysis with the MEB rheology (not shown) also shows that the choice of damage propagation scheme can also significantly affect the spatio-temporal scaling and could be used to tune this rheology against observations.

Finally, a logarithmic reduction in the spatial and temporal scaling exponents when increasing the temporal and spatial scales of the deformation estimates (i.e. $\beta \sim c_\beta \ln(T)$ and $\alpha \sim c_\alpha \ln(L)$), the so-called *space-time coupling* is achieved by all sea-ice rheologies, regardless of the original spatio-temporal resolution of the model runs (Figures 6, 7, 10, 11, c and d). This indicates that the simulated deformation fields appear less and less localized as the spatial and temporal scales are increased, consistent with the smoothing of deformation features when averaged at larger and larger scales. The strength of

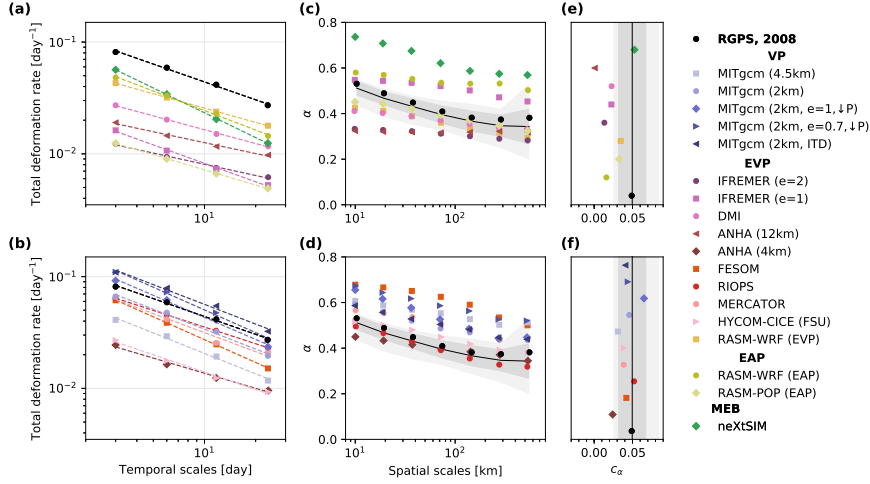


Figure 11. Same as Figure 10 for total deformation rates in January-February-March 2008.

the observed RGPS coupling, evaluated by the coupling constants c_β and c_α (i.e. the slope in semi-log plot), is also well reproduced by all rheologies at both low- and high-resolution (Figures 6, 7, 10, 11, e and f). Runs for which the space-time coupling is systematically absent or very weak (e.g. IFREMER $e=2$ and ANHA 12 km) are low-resolution EVP runs and already have smoother deformation fields to start with. Marsan and Weiss (2010) suggested that a space-time coupling of sea-ice deformation scaling can emerge from brittle dynamics and a possible chain-triggering deformation mechanism similar to that observed for earthquakes. We show here that sea-ice rheologies that do not assume brittle parameterizations also reproduce such a coupling.

4.1.3 Multi-fractal analysis

As the moment q of the total deformation distribution increases, the scaling exponents $\beta(q)$ and $\alpha(q)$ also increase, given that the scaling still holds. For mono-fractal systems, the increase in localization is linear with increasing moment, while for multi-fractal systems, the increase in localization with increasing moment deviates from linearity. Multi-fractality then reflects a large variability of the scaling exponent within the field. For sea-ice deformation fields, multi-fractality can be interpreted as larger deformation rates being more localized (in space and time) than smaller deformation rates (Weiss & Dansereau, 2017; Rampal et al., 2019).

Using the universal multi-fractal formalism, the non-linear multi-fractal structure functions are described by three variables: the degree of multi-fractality μ , the degree of heterogeneity C_1 , and the fluctuation exponent H (see Eq. 16). The spatial scaling exponent of the mean total deformation rates evaluated in the previous section is equal to $\beta(1) = 1 - H$ and therefore, the larger the H , the smoother (or less localized) the field appears. Interpretation of the effects of μ and C_1 on the observable fields are less intuitive. Generally, a larger value of μ characterizes a field dominated by singularities of larger values, and a larger C_1 indicates that these singularities are more sparsely grouped (Lovejoy & Schertzer, 2007, 2013). However, for the same values of μ , C_1 , and H the field-to-field variability can be large (Lovejoy & Schertzer, 2013) and it is not straightforward to visually distinguish the effects of the different parameters. We can nonetheless identify a few general points below regarding the use of the structure functions and the multi-fractal parameters as deformation metrics for evaluating sea-ice models. Note that, while

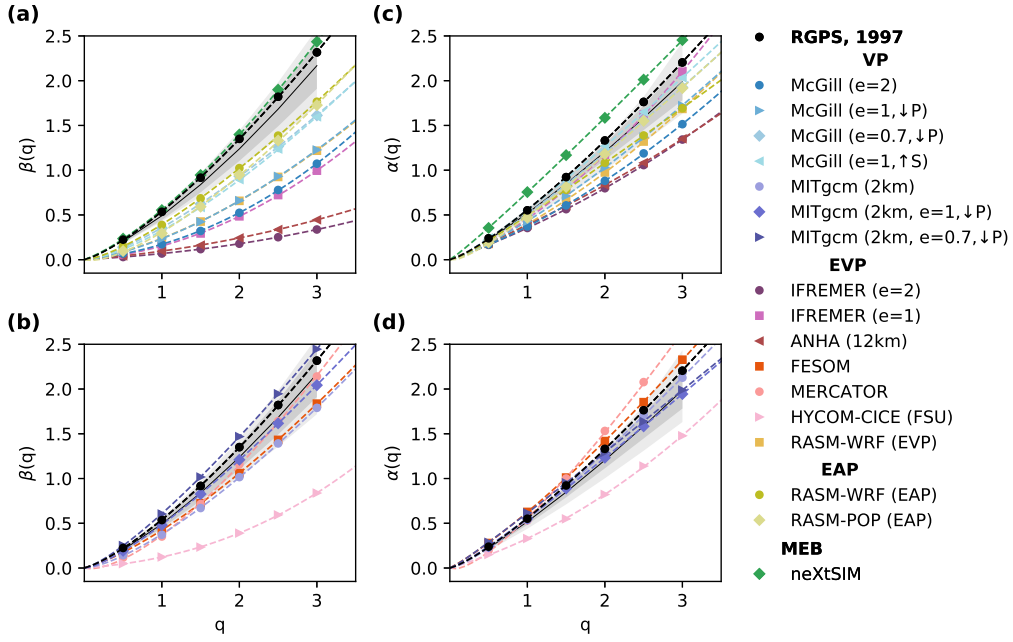


Figure 12. Left: RGPS (black) and simulated (colors) spatial structure functions $\beta(q)$ for total deformation rates estimated at $T=3$ days in January-February-March 1997. Right: Temporal structure functions $\alpha(q)$ for total deformation rates estimated at $L=10$ km in January-February-March 1997. Dashed lines are the least-square fit to Equation 16 used to derive the degree of multi-fractality μ , the degree of heterogeneity C_1 , and the fluctuation exponent H . The solid black lines, dark gray, and light gray shaded areas are the mean, standard deviation, and min/max for the entire RGPS data set. Model results are separated with low-resolution runs in top panels, and high-resolution runs in bottom panels.

the multi-fractal formalism requires $0 \leq C_1 \leq 2$ and $0 \leq \mu \leq 2$, here the least-square fits used to obtain the multi-fractal parameters are not constrained to return values in these intervals, allowing us to evaluate the validity of the multi-fractal hypothesis for the observed and simulated deformation fields.

All sea-ice rheologies reproduce non-linear structure functions in space and time, suggesting that multi-fractality (i.e. $\mu \neq 0$) and heterogeneity ($C_1 \neq 0$) are not exclusive to a specific rheology assumption (Figures 12, 13 and Figures 14, 15). In general, the conclusions of the previous section based on the scaling of the mean ($q = 1$) total deformation rates also apply to $q > 1$, with the exception that agreement with the RGPS interannual variability does not necessarily carry over to higher moments. These conclusions include higher scaling exponent for MEB and high-resolution models, lower scaling exponents for EVP runs with fewer subcycles, larger variability of spatial scaling exponents compared to temporal scaling exponents. In fact, models agreeing with the RGPS distribution for the fluctuation exponent H (i.e. for the scaling of the mean) do not necessarily agree in the other multi-fractal parameters describing the structure functions, and vice-versa (Figures 14 and 15). However, we note that the spatial and temporal multi-fractality hypothesis for RGPS observations is not robust since the distribution of the fitted degree of multi-fractality (μ) reaches values outside the theoretical range, which complicates the comparison and interpretation of the observed and simulated multi-fractal

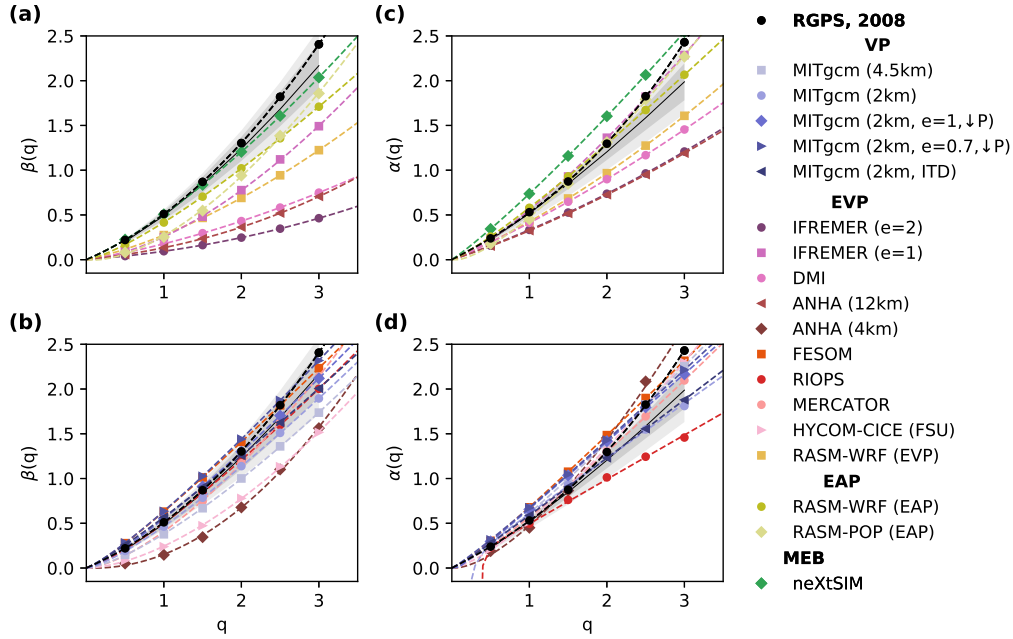


Figure 13. Same as Figure 12 for total deformation rates in January-February-March 2008

parameters (e.g. in 2008 – Figures 14 and 15). In this case, the usefulness of the multi-fractal structure functions to evaluate sea-ice deformation fields is not clear and more work is required to better understand why the multi-fractal hypothesis is not valid for certain years. Nevertheless, we note that the degree of multi-fractality (μ) for other years of the RGPS records is generally not quadratic (i.e. $\mu \neq 2$). This confirms that all three multi-fractal parameters should be used as metrics for the structure functions, as opposed to considering a fixed (e.g. quadratic) degree of multi-fractality and using only the degree of heterogeneity as a metric.

4.2 Effects of model configuration and other parameterizations

Results from the previous section show that deformation statistics have a run-to-run variability that can be as large or larger than the effects of the choice of a given sea-ice rheology. In the present section, we explore model parameterizations that could explain part of this variability.

4.2.1 Ice strength parameters

In the classical two ice-categories (E)VP rheology, the ice strength is parameterized using an elliptical yield curve and a compressive ice strength parameter P^* , which defines the maximum isotropic compressive stress that can be supported by ice for a given thickness and concentration (Hibler, 1979). The elliptical yield curve then implicitly defines the shear strength parameter S^* of the ice through the ratio of the major to minor axes, i.e. the ellipse ratio e (Bouchat & Tremblay, 2017). Calibration of the ellipse ratio and compressive ice strength parameter have usually been performed by minimizing the drift and/or thickness errors (e.g. Hibler & Walsh, 1982; Miller et al., 2006; Ungermann et al., 2017). However, the PDFs of sea-ice deformation rates are sensitive to independent changes of P^* or S^* , and therefore it has been suggested that observed RGPS

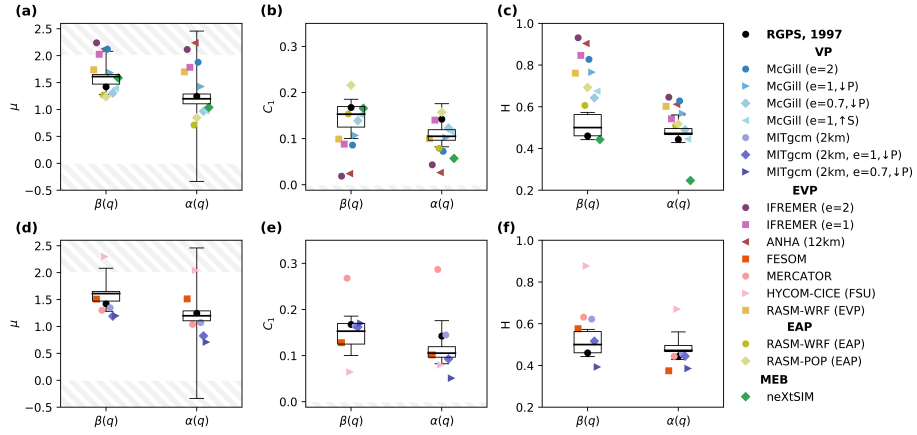


Figure 14. Multi-fractal parameters (μ , C_1 , H — see Equation 16) for the spatial structure function $\beta(q)$, and for the temporal structure function $\alpha(q)$, for runs in 1997 and RGPS inter-annual variability (boxplots). Dashed areas represent parameters outside the valid range predicted by the multi-fractal formalism. Model results are separated with low-resolution runs in top panels, and high-resolution runs in bottom panels.

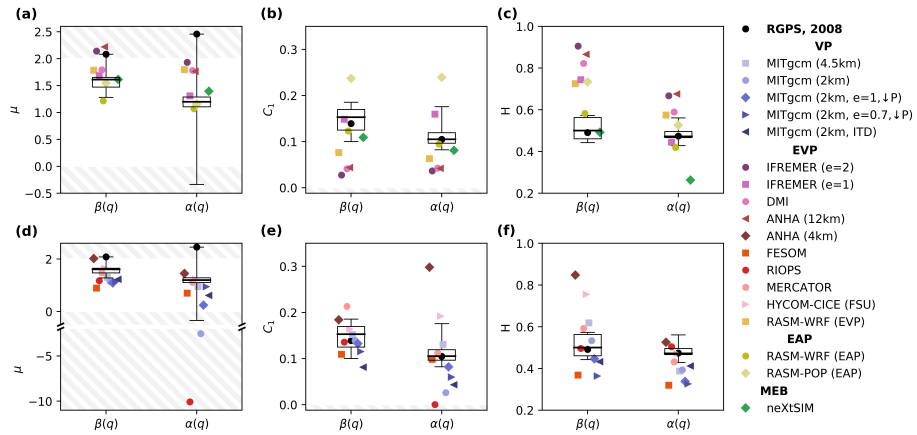


Figure 15. Same as Figure 14, for runs 2008.

PDFs of deformation rates can be used to calibrate the ice strength parameters in sea-ice models (Bouchat & Tremblay, 2017). Specifically, increasing the ratio of shear-to-compressive ice strength parameters (i.e. reducing the ellipse ratio from $e = 2$, $P^* = 27.5 \text{ kNm}^{-2}$ to $e = 1$, $P^* = 13.8 \text{ kNm}^{-1}$) significantly improved the agreement between observed and simulated PDFs of deformation rates for VP gridded deformation fields at low (10 km) resolution. Other studies using the (E)VP rheology with a reduced ellipse ratio (i.e. $0.7 \leq e \leq 1.8$) at low resolution also showed improved landfast ice and ice bridges simulation, as well as reduced ice thickness bias (Miller et al., 2005; Dumont et al., 2009; Lemieux et al., 2016). Whether these conclusions are configuration-dependent (e.g. resolution, forcing, ridging scheme, etc.) has however not been tested.

We revisit the McGill runs (same as in Bouchat & Tremblay, 2017) in order to investigate the sensitivity of the deformation statistics to the ice strength parameters with our updated deformation metrics, which now include temporal scaling, multi-fractal structure functions, and the new PDF-difference metric. We also extend this analysis to the IFREMER runs (low-resolution) and MITgcm 2-km runs (high-resolution), where only the compressive ice strength parameter P^* and the ellipse aspect ratio e were modified. At low resolution (McGill and IFREMER runs), the results confirm that increasing the ratio of shear-to-compressive strength parameter improves the agreement of all simulated deformation statistics with RGPS observations, independently of the model configuration. The PDF-difference metric reveals that reducing the ice strength in compression even lower than suggested in Bouchat and Tremblay (2017) provides a better agreement with the RGPS distributions (see e.g. McGill $e=0.7$, $\downarrow P$ in Figure 1). We also note that the spatio-temporal scaling analysis of Lagrangian trajectories with signal-to-noise ratios as weights is more conclusive than the gridded scaling analysis in Bouchat and Tremblay (2017). The results show that an increase in the shear-to-compressive strength ratio (either by reducing P^* or increasing S^*) systematically leads to spatial and temporal scaling exponents closer to those for the RGPS observations for both the McGill and IFREMER low-resolution runs (Figures 6, 7, 10, and 11). The analysis of the structure functions also reveals that the degree of heterogeneity and intermittency (C_1) in space and time is sensitive to changes in the shear-to-compressive strength ratio with the (E)VP rheology (Figures 14 and 15).

At high resolution (MITgcm 2-km runs), increasing the shear-to-compressive strength ratio can also improve the sea-ice deformation statistics (Figures 3,4,6,7,10,11,14 and 15). However, we note that the combination of ice strength parameters that provided the best model-observation agreement for McGill runs (i.e. $e = 0.7$, $P^* = 9.6$) does not result in the best agreement for the MITgcm 2-km runs. The effects of increasing the shear-to-compressive strength ratio on the degree of heterogeneity and multi-fractality at high resolution are also less clear than at low resolution. These results likely point at the intimate links that exist between the (E)VP yield curve, the deformation fields and the energy dissipation, and to the need of better understanding how sea-ice parameterizations should (or not) change with changing model resolution.

Finally, we note that the yielding shear, compressive, and tensile strength are much larger for the Mohr-Coulomb yield curve in the neXtSIM model than for typical plastic elliptical yield curves (see Table 1). In VP models at low-resolution, a higher shear strength allows the stress level to increase within the ice and to be relieved along well-defined and less frequent (more intermittent) deformation features, which helps improving the simulated deformation statistics (Bouchat & Tremblay, 2017). Whether this is also the case in the MEB rheology and could also partly explain the better deformation statistics of the neXtSIM model at low resolution compared to other (E)VP models remains to be verified.

4.2.2 Ice Thickness Distribution

The simplest way to represent the presence of ice in a continuum sea-ice model is to use two categories of ice thickness: thick ice, and thin or no ice. The ice is then characterized by its mean thickness (h) and concentration (A) per grid cell, and the ice strength is typically assumed to depend linearly on h (Hibler, 1979). However, as multiple sub-grid scale processes in the Arctic climate system are affected by the local presence of thick versus thin ice (e.g. albedo, conductive heat fluxes, etc.) it is now common practice to use an ice-thickness distribution (ITD) with more than two thickness categories (Thorndike et al., 1975). In this case, the ice strength can instead be parameterized as a function of the change in potential energy during the ridging process (Rothrock, 1975), which explicitly depends also on the thinnest ice category and on the local distribution of ice in the different thickness categories. This change in the ice strength formulation was shown to increase the spatial heterogeneity of the simulated ice strength and to significantly increase the deformation rates in convergence for thick multi-year ice in a very-low resolution ($\Delta x \sim 36$ km) coupled ice-ocean model (Ungermann et al., 2017). Hutter and Losch (2020) recently showed that using the ice strength parameterization of Rothrock (1975) with a multi-category ITD also results in a larger number (or density) of LKFs in high-resolution runs.

Here, the 2008 MITgcm 2-km runs (one with two thickness categories and the other with an ITD) allow us to investigate the effects of the ITD on the deformation statistics within the same model, in light of the new PDF-difference metric introduced in Section 4.1.1 and the updated scaling analysis with signal-to-noise ratio weights. On the one hand, we find that there is no clear improvement in the agreement of the simulated PDFs of shear rates and absolute divergence with observations when introducing an ITD at high resolution (Figure 4). On the other hand, using a multiple-category ITD significantly increases the spatial scaling exponent for the mean total deformation rate (Figure 7), apparently because there are more LKFs in the thicker pack ice (Hutter et al., 2021). We note however that the temporal scaling exponent remains unchanged by the introduction of multiple categories in the ITD (Figure 11), suggesting that the local sub-grid redistribution of ice in the ITD that can initiate the formation of new LKFs does not affect the long-range temporal correlations giving rise to the temporal scaling, or at least that the temporal effects of this process are not resolved at the 3-day scale. We also note that the spatial scaling exponents for both runs are more similar for larger moments q (Figure 13). This indicates that the multiple-category ITD mostly increases the spatial localization of smaller deformation rates. We therefore hypothesize that the effects of the ITD on the deformation statistics might be more important at lower resolution since strain rates are smaller to start with, but this remains to be verified.

We finally note that the use of an ITD in itself does not guarantee a better spatio-temporal localization of deformations. For instance, the HYCOM-CICE (FSU) runs have a five-category ITD, but the localization of the simulated deformation fields remains low compared to other high-resolution runs. In this case, too few EVP subcycles and large residual errors on the solution may again partly explain the poor localization of deformations.

4.2.3 Atmospheric forcing

Kwok (2001) showed that LKF patterns in the observed RGPS deformation fields can remain very similar for long periods of time (\sim months) suggesting that pack ice deformations occur independently of variability in the wind forcing. However, the majority of LKFs are active on much shorter time scales and LKF lifetimes show an exponential tail (Hutter et al., 2019). Thus, one can wonder about the importance of the atmospheric forcing in setting the observed and simulated small-scale deformation statistics. Given that the majority of the energy input that sets the ice cover in motion originates

from the atmospheric forcing (e.g. Steele et al., 1997; Bouchat & Tremblay, 2014), it could be expected that the simulated deformation scaling statistics are inherited from the turbulent/multi-fractal scaling properties of the atmosphere (e.g. Schmitt et al., 1994). For example, Hutter (2015) showed that the spatial scaling exponent in idealized numerical experiments depends on the spatial resolution of the reanalysis wind forcing, suggesting that the simulated small-scale deformation statistics are, in part, limited by the complexity of the imposed atmospheric forcing. However, the observed scaling properties of sea-ice deformations were shown to hold down to temporal scales much smaller than the atmospheric mesoscale or synoptic temporal scale using ship-based radar observations (Oikkonen et al., 2017). Weiss (2017) suggests this to be a confirmation that the mechanical response of the ice cover is not controlled by the atmospheric forcing, at least not at the mesoscale or synoptic temporal scale (Weiss, 2017).

Here, we note that the degree of temporal multi-fractality and heterogeneity for turbulent wind (i.e. $\mu = 1.45 \pm 0.1$, $C_1 = 0.25 \pm 0.1$; Schmitt et al., 1994) is close to that for RGPS deformation rates (see e.g. Figure 14 a,b). While this does not confirm that the observed multi-fractality of RGPS deformation rates originates from that of the wind forcing, it nonetheless shows that we cannot assume a specific lowest scale for the atmospheric forcing, such that sea-ice deformation scaling statistics could well be influenced by atmospheric forcing below the mesoscale and synoptic scale. We further note that the deformation statistics in the fully-coupled atmosphere-ice-ocean RASM-WRF (EAP) runs with higher spatial and temporal resolution of the atmospheric and oceanic components are closer to RGPS observations compared to runs with the same model but forced with an atmospheric reanalysis (i.e. RASM-POP (EAP) — see Figures 1, 2, 6, 7, 10, and 11). Larger deformation rates appear in the PDFs (especially in shear, where the PDF difference metric reduces by $\sim 50\%$), and the spatio-temporal scaling exponents for the mean total deformation rate also increase. However, we cannot firmly attribute these improvements to the increased complexity of the atmospheric forcing only, since the fully-coupled runs also have an increased number of elastic subcycles (i.e. smaller subcycling time step for the same advective time step) which suggest a better numerical convergence of their solution, although this is not directly quantifiable with the numerical implementation of the EAP rheology.

5 Discussion

In the previous sections, both plastic and brittle sea-ice rheologies have shown the potential for reproducing the observed RGPS deformation scaling statistics, even if plastic rheologies do not use specific assumptions that were hypothesized to give rise to the observed scaling of sea-ice deformations (e.g. long-range elastic interactions, damage and healing mechanism, etc. – Weiss & Dansereau, 2017). In particular, a non-zero temporal scaling, intermittency, and temporal multi-fractality is observed for practically all sea-ice models, independently of their spatial scaling. It has previously been assumed that the temporal correlations (or a certain form of *memory* resulting in time clustering of deformations) giving rise to the temporal scaling and intermittency of deformations should be inherent to the imposed sea-ice mechanical behavior (e.g. Weiss & Dansereau, 2017; Hutter et al., 2018). For instance, Weiss and Dansereau (2017) suggested that plastic sea-ice rheologies cannot reproduce temporal scaling because they do not include stress relaxation, such that temporal correlations cannot develop in their deformation fields. Well-defined LKFs in high-resolution models could also provide such a “memory” via local weakening and divergence of the ice along LKFs (Hutter et al., 2018). Here, we show that plastic sea-ice rheologies, even those without well-defined LKFs, do reproduce a strong temporal localization of deformations and a degree of temporal multi-fractality and intermittency similar to that of the observed RGPS deformation fields. The origin of the multi-fractal temporal scaling in both observed and simulated deformation fields remains to be identified. We note however that we find no significant correlation between sim-

ulated temporal scaling exponents and LKFs growth rates or lifetimes (not shown). We hypothesize that temporal correlations in the simulated deformation field could emerge from persistent synoptic atmospheric forcing at the basin scale, loading the ice and re-opening recently frozen leads, keeping the ice pack active for several days at a time followed by periods of rest. This is in agreement with RGPS observations showing that deformation of the multiyear ice pack is accommodated by long-lasting LKFs (e.g. Coon et al., 2007). This hypothesis remains to be tested in future work.

In light of the results presented in this first part of the SIREx analysis, a few recommendations for model development and implementation emerge for improving the representation of sea-ice deformation statistics by sea-ice models. First, a spatial resolution of Eulerian models higher than that of the observations is required in order to better localize the deformations and capture their heterogeneity at the observation scale. In Eulerian models, several grid cells are always required to represent a velocity discontinuity (e.g. a lead opening or a shear fracture line). Specifically, in VP finite-difference models, the number of grid points required to resolve a discontinuity forming under the same forcing conditions remains approximately the same with increasing model spatial resolution (5–7 grid points; Williams & Tremblay, 2018), leading to a spatial refinement of LKFs and an increased spatial localization of deformations with increasing resolution. The spatial resolution of Eulerian models should therefore be at least 5–7 times that of the observations for a fair comparison of their deformation field. Note that as the spatial resolution increases ($\Delta x \lesssim 100$ km), the continuum assumption (requiring the presence of a large number of ice floes within one grid cell) is technically no longer valid. However, current sea-ice models remain able to capture the observed deformation statistics because the simulated deformations are shown here to be scale-independent.

We further note that it is not expected that models (Eulerian or Lagrangian) reproduce the observed deformation statistics when run at the same nominal scale as the RGPS observation scale. The observed Lagrangian deformation fields are obtained from the motion of tracers at a 10-km spatial scale, but displacement at this scale is closely tied to processes acting on much finer scales that can act as initiation for larger-scale deformations (e.g. micro-fractures, thermal cracking and bending, etc.). These fine-scale processes are sub-grid-scale processes and are usually not resolved or parameterized by sea-ice models, with the exception of neXtSIM which uses a damage parameterization that can represent sub-grid brittle fracturing to some extent. We therefore hypothesize that including well-tuned parameterizations of the sub-grid-scale mechanical processes could also help with the representation of larger-scale sea-ice deformations. The use of a multi-category ice thickness distribution, for example, improves the simulated deformation scaling statistics and can also partly improve the LKFs statistics (see also Hutter et al., 2021). Note that a brittle fracturing parameterization (e.g. using a damage formulation) could also be implemented in plastic rheologies, which could help to better understand its role on the simulated deformation statistics.

Second, calibrating the yield curve parameters proves to be an efficient solution to improve the deformation statistics, even if sea-ice models are not run at very-high resolution or do not include sub-grid scale mechanical parameterizations. Specifically, we find that increasing the ratio of shear-to-compressive strength provides a better agreement with observed RGPS deformation statistics for both the VP and EVP rheologies. We provided here a new quantitative metric, the sum of the absolute difference of PDFs in logarithmic scale, that is useful for such a calibration of the yield curve parameters. The spatio-temporal scaling exponents of the mean total deformation rates could also be used to further calibrate the rheological model, however the usefulness of the scaling of higher moments of the deformation distribution (i.e. the structure functions) is not clear since the multi-fractality assumption is not robust for all years in the RGPS records.

Third and finally, ensuring a numerically converged solution without remaining noise appears to be critical for the small-scale deformation statistics when using an explicit numerical solver such as originally designed in the EVP and EAP rheologies, although this could not be directly assessed with the available runs. Results nonetheless suggest that using an increased number of iterations in the numerical solver along with a small dynamical time step (i.e. reducing the subcycling time step) improves the EVP deformation scaling statistics. The impact of the numerical convergence in EVP (but also in VP, EAP and MEB), and the impact of using the modified or adaptative EVP numerical schemes (i.e. mEVP or aEVP — Lemieux et al., 2012; Bouillon et al., 2013; Kimmritz et al., 2016) remains to be further evaluated.

6 Concluding Remarks

The first part of the Sea Ice Rheology Experiment (SIREx), with a total of 11 different models, 32 simulations, three different sea-ice rheologies ((E)VP, EAP, and MEB) and a wide range of other model parameterizations, allowed us to investigate how different sea-ice representations affect the deformation statistics using existing and new deformation metrics, namely, the sum of the absolute difference of observed and simulated PDFs of deformation rates, the spatio-temporal scaling exponents, and the multi-fractal parameters describing the structure functions. It is found that the sea-ice rheology, as well as the model configuration (e.g. resolution, atmospheric coupling, numerical convergence, etc.) and physical parameterizations (e.g. ITD and ice strength parameters) can affect the deformation statistics to a similar extent. For this reason, we argue that the aforementioned deformation metrics do not only evaluate the effect of the sea-ice rheology, and that it is important to analyze both the effects of the model configuration or parameterizations along with the effects of the rheological parameters in order to discuss the appropriateness of a given sea-ice rheology in terms of deformation statistics.

We find that a power-law scaling and multi-fractality of deformations in both space and time can be achieved by all sea-ice rheologies evaluated in this study, showing that these metrics are not sufficient to favor the use of a given rheology, and closing the debate on whether plastic rheologies can reproduce the observed deformation properties. However, the VP/EVP rheologies implemented in a Eulerian framework need to be run at higher resolution than that of the observations to yield spatial scaling exponents as high as those observed, because 5–7 grid cells are necessary to spatially resolve discontinuities with such a numerical scheme. It is also expected that spatial scaling exponents in agreement with the RGPS distribution could be obtained with the EAP rheology at very-high spatial resolution, given that its spatial scaling exponents are on the same order as for VP/EVP simulations at high-resolution. On the other hand, the spatial localization of MEB (brittle) simulations is larger than for the plastic rheologies when run at the same resolution as observations. Since these simulations (neXtSIM) are performed on a Lagrangian mesh that can better localize and follow discontinuities, it is not clear if the higher spatial scaling exponents are attributable only to the difference in sea-ice rheology.

Interestingly, a strong temporal scaling is better resolved by all rheologies compared to the spatial scaling, independently of the models' temporal resolution. While the origin of the observed and simulated temporal scaling remains to be identified, this confirms that there is not only one set of specific rheological assumptions that can give rise to strong temporal correlations in the deformation fields. We further note that increasing the shear-to-compressive strength ratio of the ice in elliptical plastic rheologies significantly increases the scaling exponents, while the addition of multiple ice categories in the ITD does not have a large influence on the temporal scaling. Coupling the ice model with an atmospheric model instead of forcing with a reanalysis also appears to significantly affect the temporal (and spatial) multi-fractal parameters and scaling. However, due to a different number of elastic subcycles in the runs with these variations (likely

leading to a difference in numerical convergence of the solution), we cannot firmly attribute this only to a change in the atmospheric forcing/coupling resolution.

The present study also allowed us to evaluate the usefulness of the scaling metrics to discriminate between different sea-ice models, as per SIREx’s goal. First, we showed that the decay exponent of the tail of the deformation PDFs does not efficiently characterize departure from reference PDFs and therefore cannot be used to extract information on the agreement of the simulated PDFs with observations. We therefore introduced a new quantitative metric that evaluates the sum of the bin-wise absolute differences between the observed and simulated PDFs in logarithmic scale. This metric better characterizes the ability of models to reproduce deformations as large as in RGPS observations since the logarithmic scale puts more weight on differences in the tail of the PDFs. Second, we showed that the spatio-temporal scaling of the mean total deformation rates as usually implemented does not capture differences in localization of deformations when the density of LKFs also changes between different simulations. For example, simulated deformation fields with few, but highly-localized LKFs return similarly low scaling exponents as more diffuse deformation fields. We showed that using the signal-to-noise ratios as weights in the scaling analysis (as introduced by Bouchat & Tremblay, 2020) helps to distinguish both cases and improves the interpretation of the scaling exponents as a measure of localization of deformations. This also allows the space-time coupling of the scaling exponents for the mean ($q = 1$) total deformation rates to emerge in RGPS observations (Bouchat & Tremblay, 2020) and to be used as an additional metric to evaluate the simulated deformation fields. Third, we found that the degree of multi-fractality for observed and simulated deformation fields is generally not quadratic as previously assumed, and that the multi-fractality hypothesis is not robust for all years of the RGPS records. Our results also show that multi-fractality in both space and time can be achieved without assuming specific “cascade-like” models for the deformation of the sea-ice cover, which leaves open the question of what physical/mechanical parameterizations common to all the tested sea-ice models are critical in producing the multi-fractality. In this sense, it is unclear whether the multi-fractal analysis is appropriate to calibrate or evaluate sea-ice rheologies, since the observed deformation multi-fractality could emerge from parameterizations other than the rheology (e.g. atmospheric forcing and turbulent momentum transfer).

Keeping in mind that the MEB and EAP rheologies are under-represented in the participating sea-ice models, the conclusions presented here should be tested using a larger number of experiments including more MEB and EAP runs, or ideally, by running a unique model configuration with different sea-ice rheologies. Specifically, to eliminate the potential differences associated with using a Lagrangian mesh, the deformation statistics of MEB runs implemented on a Eulerian grid (as recently done by Plante et al., 2019) should be evaluated. Nevertheless, this study shows that the (E)VP rheology — used in a majority of climate models — does generate large deformation rates that are highly localized in space and time, albeit by using a higher spatial resolution than currently used in GCMs and CMIP-type climate models. Generating large, localized deformation rates is a necessary condition for sea-ice models to achieve before their effect on the Arctic climate system can be assessed. While a thorough study of the impacts of sea-ice deformations and rheology in Global Climate Model runs remains to be performed, the analysis of LKFs statistics (and their link to ice thickness and concentration anomalies) presented in the second part of the SIREx analysis offers a complementary step to the present analysis towards improving the representation of sea ice in climate projections.

894

Appendix A Strain Rate Error Estimation

Trajectory errors and boundary-definition errors affect both the observed and simulated Lagrangian deformation estimates. Following Bouchat and Tremblay (2020), we consider only the trajectory errors to compute the signal-to-noise ratio of the deformation estimates and use this ratio as weight when averaging the deformation distribution for the scaling analysis. Trajectory errors result from uncertainty on the position of the Lagrangian trajectories used to compute the strain rates ($\dot{\epsilon}_{ij}$). When using the line integral approximations of Eq. 1-4 to evaluate the strain rates between time t and $t+\Delta t$, the signal-to-noise ratios of the total strain rate estimates ($\dot{\epsilon}_{tot}/\sigma_{\dot{\epsilon}_{tot}}$) can be approximated using the propagation of uncertainty as in Bouchat and Tremblay (2020):

$$\frac{\dot{\epsilon}_{tot}}{\sigma_{\dot{\epsilon}_{tot}}} \sim \frac{\dot{\epsilon}_{tot}}{\sqrt{2}\sigma_{\dot{\epsilon}_{ij}}}, \quad (\text{A1})$$

895

where $\sigma_{\dot{\epsilon}_{ij}}$ is the trajectory error on the strain rates, given by:

$$\sigma_{\dot{\epsilon}_{ij}}^2 = \dot{\epsilon}_{ij}^2 \left(\frac{\sigma_A^2}{A^2} \right) + \sum_{k=1}^4 \left(\frac{(x_{k+1}^j - x_{k-1}^j)^2}{4A^2\Delta t^2} \right) (\sigma_x^2 + \sigma_{x'}^2) + \sum_{k=1}^4 \left(\frac{(u_{k-1}^i - u_{k+1}^i)^2}{4A^2} \right) \sigma_x^2, \quad (\text{A2})$$

and σ_A , the error on the cell area A at time t , is defined as (e.g. Lindsay & Stern, 2003):

$$\sigma_A^2 = \frac{1}{4} \sum_{k=1}^4 \left[(x_{k+1}^j - x_{k-1}^j)^2 + (x_{k-1}^i - x_{k+1}^i)^2 \right] \sigma_x^2, \quad (\text{A3})$$

896

897

898

899

900

901

where σ_x and $\sigma_{x'}$ are the position errors at time t and $t+\Delta t$ respectively, and $(x_k^i, x_k^j) = (x_k, y_k)$ and $(u_k^i, u_k^j) = (u_k, v_k)$ are the position and velocity of the cell corner k . As the error on the strain rates is inversely proportional to the spatial and temporal scales of the strain rate estimates, the signal-to-noise ratio is the largest at larger spatial and temporal scales. Note that we have ignored timing uncertainties (i.e. σ_t) in Equation A3 above.

902

903

904

905

906

907

908

909

910

Position errors can originate from (i) geolocation errors that are due to uncertainty of the recording instrument or acquisition method, and/or (ii) tracking errors that occur when the position of tracked features on images are misidentified at the pixel level. For RGPS strain rates derived from the tracking of ice features in consecutive SAR images, we can assume that the geolocation error is zero and that the position of a tracked feature on the first SAR image at time t is always known exactly ($\sigma_x = 0$, see e.g. Bouchat & Tremblay, 2020; Dierking et al., 2020). The position of that feature on the second image at time $t+\Delta t$ is however affected by a tracking error of one pixel in the SAR images, i.e. $\sigma_{x'} = 100$ m (Lindsay & Stern, 2003).

For the reconstructed model Lagrangian trajectories, no tracking is done, but tracers are instead advected using the model velocity fields. Tracking errors are therefore zero, but geolocation errors accumulate in time with every step of the integration due to uncertainty on the model velocity fields. To see this, consider the case where the initial position of a tracer (x_0) at time $t_0 = 0$ is known perfectly (i.e. $\sigma_{x_0} = 0$). At time $t_1 = \Delta t$, the position of the advected tracer is $x_1 = x_0 + U_0\Delta t$, where U_0 is the model velocity in the x -direction at t_0 . At time $t_2 = 2\Delta t$, the position is $x_2 = x_1 + U_1\Delta t = x_0 + (U_0 + U_1)\Delta t$ and similarly, at any number n of subsequent integration steps Δt , we have:

$$x_n = x_0 + (U_0 + U_1 + \dots + U_{n-1})\Delta t. \quad (\text{A4})$$

Using the propagation of uncertainty and again neglecting timing uncertainties, the uncertainty σ_{x_n} on the position at time t_n , is therefore given by:

$$\sigma_{x_n} = \sqrt{n} \sigma_U \Delta t, \quad (\text{A5})$$

where we assume that the uncertainty on the model velocity remains the same in time (i.e. $\sigma_{U_n} = \sigma_U$ for all n). The error on the model Lagrangian trajectory positions therefore grows with the square-root of the number of integration steps. Assuming that the error on the model velocity in the y -direction is the same as in the x -direction, it is also straightforward to show that $\sigma_{y_n} = \sigma_{x_n}$.

Here, for simplicity in our calculations, we conservatively assume that all the points on the model trajectories have the largest error possible, i.e. the error of the last point after the full integration is done. We therefore fix $n = 2160$ steps (i.e. 90 days with $\Delta t = 1$ hr time steps), such that for any point along the model trajectory we have:

$$\sigma_x = \sigma_{x'} = \sigma_{x_{2160}} = (1.7 \times 10^5) \sigma_U. \quad (\text{A6})$$

The error on the ice velocity is due to an interpolation error of gridded model velocity fields to the trajectory positions, as well as to the numerical error on the dynamical solution resolved by the sea-ice models. The latter source of error depends on the model time step and spatial resolution, the choice of numerical solver and number of iterations performed to solve the non-linear dynamical equations (i.e. convergence of the solution), on the numerical regularization methods and parameterization schemes used, etc. (e.g. Lemieux et al., 2008, 2010, 2012; Bouillon et al., 2013; Kimmritz et al., 2015, 2017; Plante et al., 2019). The values of σ_U are therefore expected to vary within the participating simulations, however, those values are unknown and a complete convergence/error analysis is outside the scope of the present study. We therefore assume an upper bound of $\sigma_U = 0.006$ m/s for all simulations regardless of their specific configurations and parameterizations, which corresponds to a typical velocity error for high-resolution EVP simulations with a default number (120) of elastic subcycles and a time step of 20 minutes (Lemieux et al., 2012), and should also largely encompass the interpolation error. This corresponds to a position uncertainty of $\sigma_x \simeq 1000$ m for simulated Lagrangian trajectories. Note that this error is especially overestimated for very-high resolution models which generally have a much smaller time step and a larger number of elastic subcycles.

Acknowledgments

Conceptualization, A.B. and N.H.; Methodology, A.B. and N.H.; Resources, all authors; Data Curation, A.B.; Investigation, A.B.; Writing – Original Draft, A.B.; Writing – Review & Editing, all authors; Project administration, A.B. and N.H.

D. Dukhovskoy was funded by the DOE (award DE-SC0014378) and HYCOM NOPP (award N00014-19-1-2674). The HYCOM-CICE simulations were supported by a grant of computer time from the DoD High-Performance Computing Modernization Program at NRL SSC. The daily fields from the 0.08 HYCOM-CICE experiment are available at the HYCOM data server ftp://ftp.hycom.org/datasets/ARCC0.08/expt_11.0/data/. T. Rasmussen was funded by the Danish State through the National centre for Climate Research and by the SALIENSEAS project part of the ERA4CS programme, which is co-funded by the Innovation Fund Denmark and the Horizon 2020 Framework Programme of the European Union (Grant 690462). P. Myers was funded by the Natural Sciences and Engineering Research Council (NSERC) of Canada (RGPIN 04357 and RGPCC 433898). Experiments were run and are archived using facilities provided by Compute Canada (www.computeCanada.ca). For more details on the ANHA configuration, visit <http://knossos.eas.ualberta.ca/anha/anhatable.php>. Q. Wang was supported by the German Helmholtz Climate Initiative REKLIM (Regional

Climate Change). B. Tremblay was funded by the Natural Science and Engineering and Research Council (NSERC) Discovery Program and by the Environment and Climate Change Canada Grants & Contributions program. This work is also a contribution to the research program of Québec-Océan.

Data is available upon request.

References

- Benzi, R., Paladin, G., Parisi, G., & Vulpiani, A. (1984). On the multifractal nature of fully developed turbulence and chaotic systems. *Journal of Physics A: Mathematical and General*, 17(18), 3521.
- Bouchat, A., & Tremblay, B. (2014). Energy dissipation in viscous-plastic sea-ice models. *Journal of Geophysical Research: Oceans*, 119(2), 976–994. doi: 10.1002/2013JC009436
- Bouchat, A., & Tremblay, B. (2017). Using sea-ice deformation fields to constrain the mechanical strength parameters of geophysical sea ice. *Journal of Geophysical Research: Oceans*. doi: 10.1002/2017JC013020
- Bouchat, A., & Tremblay, B. (2020). Reassessing the Quality of Sea-Ice Deformation Estimates Derived From the RADARSAT Geophysical Processor System and Its Impact on the Spatiotemporal Scaling Statistics. *Journal of Geophysical Research: Oceans*, 125(8), e2019JC015944. (e2019JC015944 10.1029/2019JC015944) doi: <https://doi.org/10.1029/2019JC015944>
- Bouillon, S., Fichet, T., Legat, V., & Madec, G. (2013). The elastic–viscous–plastic method revisited. *Ocean Modelling*, 71. (Arctic Ocean) doi: <http://doi.org/10.1016/j.ocemod.2013.05.013>
- Bouillon, S., & Rampal, P. (2015a). On producing sea ice deformation data sets from SAR-derived sea ice motion. *The Cryosphere*, 9(2), 663–673. doi: 10.5194/tc-9-663-2015
- Bouillon, S., & Rampal, P. (2015b). Presentation of the dynamical core of neXtSIM, a new sea ice model. *Ocean Modelling*, 91, 23 - 37. doi: <http://dx.doi.org/10.1016/j.ocemod.2015.04.005>
- Ceniceros, H. D., & Hou, T. Y. (2001). An Efficient Dynamically Adaptive Mesh for Potentially Singular Solutions. *Journal of Computational Physics*, 172(2), 609 - 639. doi: <https://doi.org/10.1006/jcph.2001.6844>
- Coon, M., Kwok, R., Levy, G., Pruis, M., Schreyer, H., & Sulsky, D. (2007). Arctic Ice Dynamics Joint Experiment (AIDJEX) assumptions revisited and found inadequate. *Journal of Geophysical Research: Oceans*, 112(C11). doi: 10.1029/2005JC003393
- Courtois, P., Hu, X., Pennelly, C., Spence, P., & Myers, P. G. (2017). Mixed layer depth calculation in deep convection regions in ocean numerical models. *Ocean Modelling*, 120, 60-78. doi: 10.1016/j.ocemod.2017.10.007
- Dansereau, V., Weiss, J., Saramito, P., & Lattes, P. (2016). A Maxwell elasto-brittle rheology for sea ice modelling. *The Cryosphere*, 10(3), 1339–1359. doi: 10.5194/tc-10-1339-2016
- Dierking, W., Stern, H., & Hutchings, J. K. (2020). Estimating statistical errors in retrievals of ice velocity and deformation parameters from satellite images and buoy arrays. *The Cryosphere Discussions*, 2020, Under review. doi: 10.5194/tc-2020-8
- Dukhovskoy, D. S., Yashayaev, I., Proshutinsky, A., Bamber, J. L., Bashmachnikov, I. L., Chassignet, E. P., ... Tedstone, A. J. (2019). Role of Greenland Freshwater Anomaly in the Recent Freshening of the Subpolar North Atlantic. *Journal of Geophysical Research: Oceans*, 124(5), 3333-3360. doi: 10.1029/2018JC014686
- Dumont, D., Gratton, Y., & Arbetter, T. E. (2009). Modeling the Dynamics of

- the North Water Polynya Ice Bridge. *Journal of Physical Oceanography*, 39(6), 1448-1461. doi: 10.1175/2008JPO3965.1
- Dupont, F., Higginson, S., Bourdallé-Badie, R., Lu, Y., Roy, F., Smith, G. C., ... Davidson, F. (2015). A high-resolution ocean and sea-ice modelling system for the Arctic and the North Atlantic oceans. *Geosci. Model Dev.*, 8, 1577-1594. doi: 10.5194/gmd-8-1577-2015
- Flato, G. M., & Hibler, W. D. (1992). Modeling Pack Ice as a Cavitating Fluid. *Journal of Physical Oceanography*, 22(6), 626-651. doi: 10.1175/1520-0485(1992)022<0626:MPIAAC>2.0.CO;2
- Girard, L., Bouillon, S., Weiss, J., Amitrano, D., Fichefet, T., & Legat, V. (2011). A new modeling framework for sea-ice mechanics based on elasto-brittle rheology. *Annals of Glaciology*, 52(57), 123-132. doi: 10.3189/172756411795931499
- Girard, L., Weiss, J., Molines, J. M., Barnier, B., & Bouillon, S. (2009). Evaluation of high-resolution sea ice models on the basis of statistical and scaling properties of Arctic sea ice drift and deformation. *Journal of Geophysical Research: Oceans*, 114(C8). doi: 10.1029/2008JC005182
- Hibler, W. D. (1979). A Dynamic Thermodynamic Sea Ice Model. *Journal of Physical Oceanography*, 9, 815-946.
- Hibler, W. D., & Walsh, J. E. (1982). On Modeling Seasonal and Interannual Fluctuations of Arctic Sea Ice. *Journal of Physical Oceanography*, 12(12), 1514-1523. doi: 10.1175/1520-0485(1982)012<1514:OMSAIF>2.0.CO;2
- Hu, X., Sun, J., Chan, T., & Myers, P. G. (2018). Thermodynamic and dynamic ice thickness contributions in the Canadian Arctic Archipelago in NEMO-LIM2 numerical simulations. *The Cryosphere*, 12, 1233-1247. doi: 10.5194/tc-12-1233-2018
- Hunke, E. C., & Dukowicz, J. K. (1997). An Elastic-Viscous-Plastic Model for Sea Ice Dynamics. *Journal of Physical Oceanography*, 27(9), 1849-1867. doi: 10.1175/1520-0485(1997)027<1849:AEVPMF>2.0.CO;2
- Hunke, E. C., & Dukowicz, J. K. (2002). The Elastic-Viscous-Plastic Sea Ice Dynamics Model in General Orthogonal Curvilinear Coordinates on a Sphere-Incorporation of Metric Terms. *Monthly Weather Review*, 130, 1848-1865.
- Hutter, N. (2015). *Viscous Plastic Sea Ice Models at Very High Resolution* (MSc thesis, University of Bremen, Alfred Wegener Institute). Retrieved from <http://epic.awi.de/38870/>
- Hutter, N., Bouchat, A., Dupont, F., Dukhovskoy, D., Koldunov, K., Lee, Y., ... Wang, Q. (2021). Evaluating simulated linear kinematic features in high-resolution sea-ice simulations of the FAMOS Sea Ice rheology experiments (SIREx). *Journal of Geophysical Research: Oceans*. (Companion paper - Submitted)
- Hutter, N., & Losch, M. (2020). Feature-based comparison of sea ice deformation in lead-permitting sea ice simulations. *The Cryosphere*, 14(1), 93-113. doi: 10.5194/tc-14-93-2020
- Hutter, N., Losch, M., & Menemenlis, D. (2018). Scaling Properties of Arctic Sea Ice Deformation in a High-Resolution Viscous-Plastic Sea Ice Model and in Satellite Observations. *Journal of Geophysical Research: Oceans*, 123(1), 672-687. doi: 10.1002/2017JC013119
- Hutter, N., Zampieri, L., & Losch, M. (2019). Leads and ridges in Arctic sea ice from RGPS data and a new tracking algorithm. *The Cryosphere*, 13(2), 627-645. doi: 10.5194/tc-13-627-2019
- Kimmritz, M., Danilov, S., & Losch, M. (2015). On the convergence of the modified elastic-viscous-plastic method for solving the sea ice momentum equation. *Journal of Computational Physics*, 296, 90 - 100. doi: <https://doi.org/10.1016/j.jcp.2015.04.051>
- Kimmritz, M., Danilov, S., & Losch, M. (2016). The adaptive EVP method for solving the sea ice momentum equation. *Ocean Modelling*, 101, 59 - 67. doi:

- https://doi.org/10.1016/j.ocemod.2016.03.004
- Kimmritz, M., Losch, M., & Danilov, S. (2017). A comparison of viscous-plastic sea ice solvers with and without replacement pressure. *Ocean Modelling*, 115, 59–69. doi: https://doi.org/10.1016/j.ocemod.2017.05.006
- Koldunov, N. V., Danilov, S., Sidorenko, D., Hutter, N., Losch, M., Goessling, H., ... Jung, T. (2019). Fast EVP Solutions in a High-Resolution Sea Ice Model. *Journal of Advances in Modeling Earth Systems*, 11(5), 1269–1284. doi: https://doi.org/10.1029/2018MS001485
- König Beatty, C., & Holland, D. M. (2010). Modeling Landfast Sea Ice by Adding Tensile Strength. *Journal of Physical Oceanography*, 40(1), 185–198. doi: 10.1175/2009JPO4105.1
- Kreyscher, M., Harder, M., Lemke, P., & Flato, G. M. (2000). Results of the Sea Ice Model Intercomparison Project: Evaluation of sea ice rheology schemes for use in climate simulations. *Journal of Geophysical Research: Oceans*, 105(C5). doi: 10.1029/1999JC000016
- Kwok, R. (1998). The RADARSAT Geophysical Processor System. In C. Tsatsoulis & R. Kwok (Eds.), *Analysis of SAR Data of the Polar Oceans* (pp. 235–257). Springer-Verlag.
- Kwok, R. (2001). Deformation of the Arctic Ocean Sea Ice Cover between November 1996 and April 1997: A Qualitative Survey. In *Iutam symposium on scaling laws in ice mechanics and ice dynamics* (pp. 315–322). Springer Netherlands.
- Lemieux, J.-F., Dupont, F., Blain, P., Roy, F., Smith, G. C., & Flato, G. M. (2016). Improving the simulation of landfast ice by combining tensile strength and a parameterization for grounded ridges. *Journal of Geophysical Research: Oceans*, 121(10). doi: 10.1002/2016JC012006
- Lemieux, J.-F., Knoll, D. A., Tremblay, B., Holland, D. M., & Losch, M. (2012). A comparison of the Jacobian-free Newton–Krylov method and the EVP model for solving the sea ice momentum equation with a viscous-plastic formulation: A serial algorithm study. *Journal of Computational Physics*, 231(17), 5926–5944. doi: https://doi.org/10.1016/j.jcp.2012.05.024
- Lemieux, J.-F., Tremblay, B., Sedláček, J., Tupper, P., Thomas, S., Huard, D., & Auclair, J.-P. (2010). Improving the numerical convergence of viscous-plastic sea ice models with the Jacobian-free Newton–Krylov method. *Journal of Computational Physics*, 229. doi: 10.1016/j.jcp.2009.12.011
- Lemieux, J.-F., Tremblay, B., Thomas, S., Sedláček, J., & Mysak, L. A. (2008). Using the preconditioned Generalized Minimum RESidual (GMRES) method to solve the sea-ice momentum equation. *Journal of Geophysical Research*, 113(C10004). doi: 10.1029/2007JC004680
- Lindsay, R. W., & Stern, H. L. (2003). The RADARSAT Geophysical Processor System: Quality of Sea Ice Trajectory and Deformation Estimates. *Journal of Atmospheric and Oceanic Technology*, 20(9), 1333–1347.
- Lovejoy, S., & Schertzer, D. (1995). How bright is the coast of Brittany. *Fractals in Geoscience and Remote Sensing*, 102–151.
- Lovejoy, S., & Schertzer, D. (2007). Scale, Scaling and Multifractals in Geophysics: Twenty Years on. In *Nonlinear dynamics in geosciences* (pp. 311–337). Springer New York.
- Lovejoy, S., & Schertzer, D. (2013). *The weather and climate: emergent laws and multifractal cascades*. Cambridge University Press.
- Madec, G. and NEMO System Team. (2019). NEMO ocean engine (Computer software manual No. 27). Zenodo. doi: 10.5281/zenodo.1464816
- Madsen, K. S., Rasmussen, T. A. S., Ribergard, M. H., & Ringgaard, I. M. (2016). High resolution sea ice modelling and validation of the Arctic with focus on south Greenlandic waters, 2004–2013. *Polarforschung*, 85.
- Marsan, D., Stern, H., Lindsay, R., & Weiss, J. (2004). Scale Dependence and Local-

- ization of the Deformation of Arctic Sea Ice. *Phys. Rev. Lett.*, 93, 178501. doi: 10.1103/PhysRevLett.93.178501
- Marsan, D., & Weiss, J. (2010). Space/time coupling in brittle deformation at geophysical scales. *Earth and Planetary Science Letters*, 296(3-4), 353-359. doi: 10.1016/j.epsl.2010.05.019
- Miller, P. A., Laxon, S. W., & Feltham, D. L. (2005). Improving the spatial distribution of modeled Arctic sea ice thickness. *Geophysical Research Letters*, 32(18). (L18503) doi: 10.1029/2005GL023622
- Miller, P. A., Laxon, S. W., Feltham, D. L., & Cresswell, D. J. (2006). Optimization of a Sea Ice Model Using Basinwide Observations of Arctic Sea Ice Thickness, Extent, and Velocity. *Journal of Climate*, 19(7). doi: 10.1175/JCLI3648.1
- Mohammadi-Aragh, M., Goessling, H. F., Losch, M., Hutter, N., & Jung, T. (2018). Predictability of Arctic sea ice on weather time scales. *Scientific reports*, 8.
- Muilwijk, M., Ilicak, M., Cornish, S. B., Danilov, S., Gelderloos, R., Gerdes, R., ... Wang, Q. (2019). Arctic Ocean Response to Greenland Sea Wind Anomalies in a Suite of Model Simulations. *Journal of Geophysical Research: Oceans*, 124(8), 6286-6322. doi: https://doi.org/10.1029/2019JC015101
- Oikonen, A., Haapala, J., Lensu, M., Karvonen, J., & Itkin, P. (2017). Small-scale sea ice deformation during N-ICE2015: From compact pack ice to marginal ice zone. *Journal of Geophysical Research: Oceans*, 122(6), 5105-5120. doi: 10.1002/2016JC012387
- Plante, M., Tremblay, B., Losch, M., & Lemieux, J.-F. (2019). The material properties of ice bridges in the Maxwell Elasto-Brittle rheology. *The Cryosphere Discussions*, 2019, 1-50. doi: 10.5194/tc-2019-210
- Rampal, P., Bouillon, S., Ólason, E., & Morlighem, M. (2016). neXtSIM: a new Lagrangian sea ice model. *The Cryosphere*, 10(3), 1055-1073. doi: 10.5194/tc-10-1055-2016
- Rampal, P., Dansereau, V., Olason, E., Bouillon, S., Williams, T., & Samaké, A. (2019). On the multi-fractal scaling properties of sea ice deformation. *The Cryosphere Discussions*, 2019, 1-45. doi: 10.5194/tc-2018-290
- Rampal, P., Weiss, J., Marsan, D., Lindsay, R., & Stern, H. (2008). Scaling properties of sea ice deformation from buoy dispersion analysis. *Journal of Geophysical Research: Oceans*, 113(C3). doi: 10.1029/2007JC004143
- Rothrock, D. A. (1975). The energetics of the plastic deformation of pack ice by ridging. *Journal of Geophysical Research (1896-1977)*, 80(33). doi: 10.1029/JC080i033p04514
- Schmitt, F., Schertzer, D., Lovejoy, S., & Brunet, Y. (1994). Estimation of universal multifractal indices for atmospheric turbulent velocity fields. In *Fractals in natural sciences* (p. 274-281). doi: 10.1142/9789814503792_0025
- Schulson, E. M. (2004). Compressive shear faults within arctic sea ice: Fracture on scales large and small. *Journal of Geophysical Research: Oceans*, 109(C7). (C07016) doi: 10.1029/2003JC002108
- Spren, G., Kwok, R., Menemenlis, D., & Nguyen, A. T. (2017). Sea-ice deformation in a coupled ocean-sea-ice model and in satellite remote sensing data. *The Cryosphere*, 11(4), 1553-1573. doi: 10.5194/tc-11-1553-2017
- Steele, M., Zhang, J., Rothrock, D., & Stern, H. (1997). The force balance of sea ice in a numerical model of the Arctic Ocean. *Journal of Geophysical Research: Oceans*, 102(C9), 21061-21079. doi: 10.1029/97JC01454
- Stern, H. L., & Lindsay, R. W. (2009). Spatial scaling of Arctic sea ice deformation. *Journal of Geophysical Research: Oceans*, 114(C10). (C10017) doi: 10.1029/2009JC005380
- Stroeve, J., Barrett, A., Serreze, M., & Schweiger, A. (2014). Using records from submarine, aircraft and satellites to evaluate climate model simulations of Arctic sea ice thickness. *The Cryosphere*, 8(5). doi: 10.5194/tc-8-1839-2014
- Thorndike, A. S., Rothrock, D. A., Maykut, G. A., & Colony, R. (1975). The

- thickness distribution of sea ice. *Journal of Geophysical Research*, 80(33), 4501–4513. doi: 10.1029/JC080i033p04501
- Tsamados, M., Feltham, D. L., & Wilchinsky, A. V. (2013). Impact of a new anisotropic rheology on simulations of Arctic sea ice. *Journal of Geophysical Research: Oceans*, 118(1), 91–107. doi: 10.1029/2012JC007990
- Ungermann, M., Tremblay, L. B., Martin, T., & Losch, M. (2017). Impact of the ice strength formulation on the performance of a sea ice thickness distribution model in the Arctic. *Journal of Geophysical Research: Oceans*. doi: 10.1002/2016JC012128
- Wang, Q., Danilov, S., Jung, T., Kaleschke, L., & Wernecke, A. (2016). Sea ice leads in the Arctic Ocean: Model assessment, interannual variability and trends. *Geophysical Research Letters*, 43(13), 7019–7027. (2016GL068696) doi: 10.1002/2016GL068696
- Weiss, J. (2008). Intermittency of principal stress directions within Arctic sea ice. *Phys. Rev. E*, 77. doi: 10.1103/PhysRevE.77.056106
- Weiss, J. (2017). Exploring the “solid turbulence” of sea ice dynamics down to unprecedented small scales. *Journal of Geophysical Research: Oceans*, 122(8). doi: 10.1002/2017JC013236
- Weiss, J., & Dansereau, V. (2017). Linking scales in sea ice mechanics. *Philosophical Transactions of the Royal Society A: Mathematical, Physical and Engineering Sciences*, 375(2086). doi: 10.1098/rsta.2015.0352
- Wilchinsky, A. V., & Feltham, D. L. (2006). Modelling the rheology of sea ice as a collection of diamond-shaped floes. *Journal of Non-Newtonian Fluid Mechanics*, 138(1), 22 – 32. doi: https://doi.org/10.1016/j.jnnfm.2006.05.001
- Williams, J., & Tremblay, L. B. (2018). The dependence of energy dissipation on spatial resolution in a viscous-plastic sea-ice model. *Ocean Modelling*, 130, 40 – 47. doi: https://doi.org/10.1016/j.ocemod.2018.08.001
- Zhang, J., & Rothrock, D. A. (2005). Effect of sea ice rheology in numerical investigations of climate. *Journal of Geophysical Research: Oceans*, 110(C8). doi: 10.1029/2004JC002599